

The Spatial Distribution of the λ Orionis Pre-Main-Sequence Population

Christopher J. Dolan

and

Robert D. Mathieu

*Department of Astronomy, University of Wisconsin–Madison, 475 North Charter Street,
Madison, WI 53706*

dolan@astro.wisc.edu; mathieu@astro.wisc.edu

ABSTRACT

The λ Ori star-forming region presents a snapshot of a moderate-mass giant molecular cloud 1–2 Myr after cloud disruption by OB stars, with the OB stars, the low-mass stellar population, remnant molecular clouds, and the dispersed gas all still present. We have used optical photometry and multi-object spectroscopy for lithium absorption to identify 266 PMS stars in 8 degrees² of the region. We also present new Strömgren photometry for the massive stars, from which we derive a distance of 450 pc and a turnoff age of 6–7 Myr. Using these parameters and pre-main-sequence evolutionary models, we map the star-formation history of the low-mass stars. We find that low-mass star formation started throughout the region at about the same time as the birth of the massive stars, and thereafter the birth rate accelerated. Within the last 1–2 Myr star-formation ceased in the center of the star-forming region, near the concentration of OB stars, while it continues in dark clouds 20 pc away. We suggest that a supernova 1–2 Myr ago destroyed the molecular cloud core from which the OB stars formed, but did not terminate star formation in more distant reaches of the giant molecular cloud. We find no secure evidence for triggered or sequential star formation in the outer molecular clouds. The global star formation of the λ Ori region has generated the field IMF, but local star formation in sub-regions shows large deviations from the expected ratio of high- to low-mass stars.

Subject headings: Stars: pre-main sequence — Stars: formation

1. Introduction

To simplify the analysis of a cluster or association of stars, one often assumes that all the stars formed at the same time, at the same place and/or under the same conditions. Of course, the

formation of a star is a complex process that depends on the nature of the local medium and may be influenced by the presence of other forming stars in the vicinity. In the past decade, the number of known pre-main-sequence (PMS) stars has grown enormously, allowing robust quantitative tests of the coevality, cospatiality and homogeneity of star formation processes in a variety of regions.

One of the most extensive of such tests is the analysis of the Orion Nebula Cluster by Hillenbrand (1997). She found a tendency for the youngest stars to be located in the cluster center, near the most massive stars. On the contrary, in the Upper Scorpius OB association Preibisch & Zinnecker (1999) demonstrated that the stars of all masses formed at the same time and place. They attributed the coevality to abrupt triggering of star formation by an external supernova shock wave and subsequent termination by cloud dispersal via winds and radiation from massive members of the star-forming region.

However, the homogeneity of Upper Sco seems to be very different from other star-forming regions. Palla & Stahler (2000) revisited the age distribution of eight star-forming regions and found that in all except Upper Sco formation began slowly several Myr ago and has accelerated to the present day. They noted that Upper Sco is the only region in their sample lacking molecular gas today. Similarly, Wichmann et al. (1997) found that in Lupus the mean age is lower for stars projected on dark cloud versus those away from the clouds.

The non-cospatiality of star-formation has become especially well-known due to the discoveries of the the ROSAT All-Sky Survey (RASS). The RASS found a huge number of PMS stars not cospatial with previously-known PMS stars (see Guillout et al. 1998). Feigelson (1996) reviewed this dispersed population and considered several explanations of how these stars came to be so far from the present-day clouds and their young neighbors. Many authors (e.g. Briceño et al. 1997; Alcalá, et al. 2000) considered that the observed PMS stars may be the superposition of multiple populations along the line of sight.

The λ Orionis star-forming region is an ideal laboratory for further study of how stars are born in a complex environment. One of the most interesting features of this region is the segregation of the classical T Tauri stars (CTTSs) from their high-mass neighbors. The Duerr, Imhoff & Lada (1982, hereafter DIL) survey for CTTSs, i.e., stars with strong $H\alpha$ emission, suggested that the low-mass stars were preferentially found on the edges of the star-forming complex. Gomez & Lada (1998) showed that the OB stars clustered at the center were a distinct spatial population from the two concentrations of DIL $H\alpha$ stars projected on the Barnard 30 and 35 dark clouds at the periphery. DIL conjectured that this spatial pattern is consistent with sequential star formation, where an expanding H II region originating at the OB stars triggered the birth of the peripheral PMS stars.

More recently, the RASS has detected a substantial number of X-ray-bright PMS candidates in the λ Ori region. As reported by Sterzik et al. (1995), these stars do not coincide with the B30 and B35 clouds as did the DIL stars. Instead, the density maximum is projected at the same position as the OB star concentration, where DIL found very few PMS stars. Further observations by Alcalá

et al. (1996), Magazzù et al. (1997) and Neuhäuser et al. (1997) proved that many of these X-ray sources are PMS stars lacking the large $H\alpha$ emission profiles seen by DIL. These discoveries revealed the large bias in the DIL emission survey against weak-lined T Tauri stars (WTTSs), i.e., PMS stars lacking strong $H\alpha$ emission. Thus, the DIL conjecture was based on an incomplete picture.

To investigate the population of PMS stars very near the OB stars, Dolan & Mathieu (1999, hereafter Paper I) performed a new survey using lithium as an unbiased diagnostic of youth and membership. This survey included only the central 1% of the star-forming region, yet revealed 70 new PMS stars, almost as many as had been discovered previously in the entire association. They showed that many of these stars are extremely young, despite a remarkable lack of $H\alpha$ emission, further questioning the DIL interpretation of sequential star formation. Using this sample, they studied the low-mass age distribution in the context of the ages and kinematics of the OB stars. The results were dependent on the choice of PMS stellar evolution model: the D’Antona & Mazzitelli (1997, 1998, hereafter collectively DM98) model indicates a recent increase in the star formation rate, while the Baraffe et al. (1998, hereafter BCAH98) model suggests most of the formation occurred at an earlier date and today the birth rate has dropped nearly to zero. However, both models agree that very few PMS stars formed prior to the birth of the B stars (Murdin & Penston 1977, about 6 Myr ago).

What does this say about the process of star birth? Do massive stars have a significant effect on the formation history of low-mass stars or would the age distribution look the same even if the massive stars did not exist? To answer this question, we have extended the Paper I survey to include a larger fraction of the star-forming region, both near to and far from the OB stars. Our goal is to study the PMS stars both as a function of radius from their massive neighbors and as an entire population.

To do this, we present results from a new photometric survey, a large extension to our WIYN¹ spectroscopic survey, and new Strömgren photometry for the population of OB stars. With these data we have identified and analyzed a sample of PMS stars covering roughly a diameter across the star-forming region. Additionally, we have improved the distance estimate to the association via the massive stars. We use these results to compute ages and masses for the young stellar population in order to deduce the star formation history of the region.

2. Data

Our procedure for identifying and studying the young population of the λ Ori star-forming region is similar to that described in Paper I: (1) obtain broad-band photometry of fields of interest, (2) select PMS candidates from R versus $R-I$ CMDs, (3) obtain spectra for these candidates, (4)

¹The WIYN Observatory is a joint facility of the University of Wisconsin-Madison, Indiana University, Yale University, and the National Optical Astronomy Observatories.

use lithium absorption to identify association members, and (5) assume a common distance for members to compute ages and masses by comparison with PMS model evolution tracks. These steps are described in the subsequent sections.

2.1. Photometry of Low-Mass Stars

In Paper I we restricted our photometric survey to a single 1° diameter field around λ Ori in the center of the star-forming region. In this work we have dramatically expanded the scope of the survey. In winter 1998–99, we used the $8K \times 8K$ Mosaic Imager on the KPNO 0.9m telescope to commence a photometric survey of the entire λ Ori star-forming region. We intended the survey to cover the entire H II region, but poor weather in our seven-night run of December 1998 only allowed us to observe 12 of the 76 planned fields in *BVRI*. K. Stassun generously acquired 8 more fields for us with the same instrument in January 1999. This allowed us to finish the highest-priority portion, which we selected to include a strip roughly along a diameter of the star-forming region extending from the B30 to B35 dark clouds. We chose this particular diameter to roughly trace the CTTS-rich strip noted by DIL. We also started imaging our second-priority fields coinciding with archival ROSAT targets.

We reduced the Mosaic images with IRAF-MSCREED, closely following the V2.0 (Sep98) guidelines. For each field, we had obtained three exposures in each filter dithered diagonally one arcminute from each other. These three exposures were registered astrometrically using MSC-CMATCH with star coordinates from the USNO-A2.0 catalog (Monet et al. 1996). These images were resampled to the sky tangent plane and combined to cover the inter-chip gaps. It is worth noting that since we used three dithered images instead of the recommended five, a small subset of stars (about 3%) may suffer a loss in signal-to-noise due to missing data in one of the three images. A smaller subset (0.1%) suffer a larger loss where the gaps of two of the three images overlap. As in Paper I, we did not attempt point source detection on these images. Instead, we selected all stars brighter than $R = 17$ from the USNO-A2.0 catalog and performed aperture photometry at the locations indicated by the USNO coordinates. We then calibrated the stars to the Johnson-Kron-Cousins system via standards from Landolt (1983, 1992). The resulting data consist of *BVRI* photometry for 5000 to 10000 stars per degree². We will hereafter refer to these data as the 1998 photometry, to distinguish from the 1999 photometry described below.

We received an additional 5.5 nights in December 1999 to continue the photometric survey. This time, we made improvements to our survey technique in the following two ways. First, we changed our image tiling pattern over the region to force the fields to overlap to a greater degree. This has allowed us to make more detailed comparisons of the photometric quality from field to field. The result is that we needed 83 instead of 76 fields to tile roughly the same region. Second, we increased the exposure time by a factor of three in *VRI* and a factor of two in *B*. This caused us to saturate many stars brighter than $R = 10$ or 11, but this does not interfere with our desired bright limit of $R = 12$ (discussed below) while significantly improving the signal-to-noise ratio of our

faintest stars of interest. The drawback of these two changes is that the survey’s total required time increased. To partially compensate for this, we elected only to obtain B images for a subset of fields: those observed spectroscopically in 1998 and those which appear to have substantial molecular gas, and thus may suffer higher extinction. Several nights of photometric weather allowed us to observe 61 of 83 fields in VRI and 21 fields in B . We selected as highest priority fields which had been observed in 1998, in order to improve the photometry. Other high priority fields were selected in regions covered by ROSAT archive data and a swath tracing the B223 cloud in the southeast. The locations of the VRI fields are shown in Figure 1.

The 1999 photometric data were reduced by a process similar to that used on the 1998 data, except for a few details. First, we used the updated V3.2.3 of IRAF-MSCREED which corrects a few systematic effects not covered in V2.0. More significantly, we used twilight flats instead of dome flats which yielded a better vignetting correction. Finally, we computed photometry on all USNO A2.0 stars down to USNO $R = 18$ instead of 17 to take advantage of our longer exposure times.

With a survey this large, we were not able to observe most stars on multiple nights. Thus, to characterize our measurement error we rely on three properties of our survey: (1) each field has three dithered images per filter taken in rapid succession which let us study internal and random error, (2) adjacent fields overlap by as much as $5'$ which let us search for night-to-night effects, and (3) many of the 1999 fields are coincident with the 1998 fields allowing another comparison. We begin with the higher-quality 1999 data and progress to the 1998 data in turn.

For each reduced field, we performed aperture photometry on each of the three exposures per filter as well as on the combined image. We examined the magnitude difference as a function of magnitude for stars found in any two of the three images. We computed statistics on the distribution of differences for stars with R magnitudes between 12 and 16 using a Gaussian inversion technique² to reject outliers. Performing this test on 35 of the fields observed in 1999, we found the following categories of photometric error for bright, intermediate and faint stars. For stars brighter than $R = 15.5$, we find a photometric dispersion which is constant. For this case, we find a mean scatter around zero of the VRI magnitude differences to be 0.023 ± 0.003 mag. Correcting to a single exposure (by dividing by $\sqrt{2}$), our *internal* limiting photometric precision limit is 0.016 mag for the 1999 data. We find essentially the same value for all three VRI filters. Stars with $15.5 < R < 17$ are photon-limited, such that their photometric dispersion is proportional to $1/\sqrt{N}$. Faint stars with $R > 17$ are background-limited as the sky noise becomes dominant.

The second test we performed compared the photometry of stars in the overlapping regions between adjacent fields. This test used our fully-reduced photometry instead of the per-exposure photometry used in the test described above. However, the following tests were performed on the edges of the chips where effects like vignetting and non-constant plate scale have the most

²For details of this technique, also called a “probit plot”, see for example van Altena et al. (1988) or Lutz & Uppgren (1980)

significance. Ideally these effects were removed during data reduction, but in practice we found that our poorest photometry comes from these regions. Thus, we consider the overlap-region tests to be a conservative means for estimating photometric quality.

For the subsequent analysis, we weight the results for each overlap region by the number of stars contained within it in the range of $11 < R < 16$. For each overlapping pair we compute a mean photometric offset as well as the dispersion around that offset, using the same Gaussian inversion technique used in the previous test. We found that the 20 fields overlapping east-west are well behaved with offsets in all three filters of 0.001 (median) or 0.000 (mean) mag. The 21 north-south overlapping fields, on the other hand, have a mean offset of 0.048 mag in the sense that the north edge of the south-most field is routinely fainter than the south edge of the north-most field for the same stars. The 1σ dispersion of the mean offsets is nearly the same for east-west and north-south pairs (0.021 and 0.024 mag respectively).

We do not fully understand the source of the anomalous north-south offset, but we note that the offset correlates with distance from the edge of the CCD within the overlap region. Fitting this correlation and removing it, we find that we can reduce the photometric difference dispersion in the overlap region by almost a factor of two. Thus, we suspect it is a correctable problem. However without external photometry as a check, we do not know which of the two overlap strips is in error. Also, we only have information about the overlap regions (about 30% of the CCD area) Thus, we take a simpler approach: where we have more than one observation of a star, we average the photometry to produce the final data set. This does not entirely correct the offset problem, but certainly reduces it.

The dispersion of the differences was similar for the north-south and east-west overlapping neighbors. Combining these data for 41 overlapping regions, we find a mean dispersion of 0.041 mag and a median of 0.038 mag. The standard deviation of the dispersion values for each field is 0.011 mag, suggesting that photometric quality varies by $\pm 25\%$ from field to field. Correcting the mean dispersion to a single field, we adopt a photometric precision of 0.029 mag for V , R and I filters.

Finally, our third test compares the 1999 and 1998 photometry. We examined 10 fields observed in both years, primarily those aligned with the WIYN-Hydra fields described below. Following procedures described above, we found a mean offset of 0.001 ± 0.030 mag. The mean dispersion around the offset is slightly different for each filter: 0.071 ± 0.007 mag for V , 0.066 ± 0.04 for R and 0.063 ± 0.004 for I . Note that this dispersion is much larger than the 1999 data considered alone. We attribute this difference to the shorter exposure times in 1998 and the use of twilight flat fields instead of dome flats in 1999. Subtracting the 1999 dispersion (0.029 mag) in quadrature we find that the 1998 photometry has an internal precision of 0.065, 0.059 and 0.056 mag for V , R and I respectively. These larger errors affect our photometric target selection, but do not affect our conclusions since we use the 1999 photometry for all computations.

2.2. Spectroscopy of Low-Mass Stars

Using the photometry described above, we selected stars which were promising candidate PMS members of the λ Ori association. For this step, we followed a similar technique to that used in Paper I. First we selected all objects with $12 < R < 16$. From that sample we selected stars redder than a 30 Myr isochrone, interpolated from the Alexander/CM tracks of D’Antona & Mazzitelli (1994) at the Murdin & Penston (1977) distance of 400 pc. We reddened these tracks to match the $E_{B-V} = 0.12$ measurement for λ Ori by Diplas & Savage (1994) (namely $A_R = 0.27$ and $E_{R-I} = 0.097$, assuming $R_V = 3.1$). Nearly all of our candidate selection was performed with our lower-quality 1998 photometry since the newer data were not yet available. Consequently, the boundaries of the selection region are slightly blurred when viewed with the 1999 photometry. However when we had fibers available for additional targets, we observed stars brighter and fainter than than our magnitude limits. Thus, the blurring is most apparent at our blue limit.

We selected targets from 11 fields to observe with WIYN Multi-Object Spectrograph (MOS). They were chosen to roughly span a diameter across the star-forming region with an emphasis on regions with many DIL stars and dense molecular gas. For the winters of 1998–1999 and 1999–2000, we were granted 6.5 nights on WIYN via the Wisconsin TAC as well as 4 nights from the NOAO TAC via the WIYNQ project. During this time, we completed our observations for 9 of the 11 target fields and started the last two. Our instrument setup and our data reduction process are identical to those described in Paper I. We derive measurements of lithium $\lambda 6708$ and $H\alpha$ equivalent width as well as a radial velocity from each spectrum.

Our data set consists of 4177 spectra of 3618 stars (including 612 spectra of 537 stars from Paper I). We detected lithium $\lambda 6708$ absorption in 648 stars, about 18% of our sample. Of these, 266 showed “strong” lithium absorption indicative of youth (defined as $W_\lambda(\text{Li}) \geq 0.2\text{\AA}$; see § 4.2). Thus the efficiency of this search technique is 7%. The location of these latter 266 stars are displayed in Figure 2.

In Table 1 we present updated coordinates and photometry for the stars presented in Paper I. This new table differs from its predecessor in that it adds an additional identifier for each stars, and in that it uses USNO-A2.0 coordinates instead of the obsolete A1.0 data, wherever possible. The photometry presented is from 1999 with one noted exception.

In Table 2 we present data for the 194 strong lithium stars not previously presented in Paper I. The star identifiers in the first two columns follow the pattern from the previous table. The coordinates in the third column (which are used to construct the second identifier) comes from the USNO-A2.0 catalog. The next three columns are V , $V-R$ and $R-I$ photometry measured in 1999 unless specified otherwise. The following three columns present our spectroscopic data: lithium equivalent width, $H\alpha$ equivalent width and stellar radial velocity. The last columns are ages and masses, which are discussed in § 5.1 below.

As in Paper I, we compute velocities by cross-correlation using either the Sun or HD 95735

(M2V). We chose the proper template to use by looking for molecular bands in the spectra. We made this choice blind to the presence or absence of lithium absorption, and used the solar template whenever there was doubt. A notable result of this selection is that 95% (127 of 134) of the stars we identified as M stars turned out to have strong lithium. Thus, nearly half (127/266) of the strong-lithium stars are M stars. None of the weak-lithium stars were flagged as M stars, while only 7 of the 2970 non-lithium stars are M spectral type.

With our larger sample of stars, we have re-examined our radial-velocity precision. Looking at the 336 stars with more than one high-quality velocity measurement (IRAF FXCOR cross-correlation height greater than 0.35), we find a median sigma of 0.57 km s^{-1} . (this estimate of our precision is more meaningful than the value of 1.2 km s^{-1} derived from the mode of the velocity sigma distribution in Paper I).

Our completeness is almost completely determined by which objects we chose to observe with WIYN MOS. As stated above, we used the inferior 1998 photometry to select targets, which caused us to miss some targets near the edge of the selection box. Additionally, we missed a small number of stars in slightly crowded regions since WIYN Hydra fibers cannot point at two stars closer than $37''$ at one time. To assess our total completeness, we counted the number of stars that should have been in our selection box using the 1999 photometry. We contrasted that with the number of those stars which were actually observed spectroscopically. The results, broken down by field are shown in Table 3. (For reference we also include in this table the number of PMS stars detected in our survey as well as the number of $\text{H}\alpha$ stars detected by DIL, broken down by field.) Excluding the two unfinished fields (1 and 3) the total completeness is 91.1%. Half of the missed stars are within 0.1 mag of our blue limit, where the field is richest. As we discuss below, there are almost no PMS stars in this region, so our PMS completeness is about 96%.

We note that intrinsic photometric variability of the stars near the edges of our photometric survey limits is not a large contributor to incompleteness. Only 1.5% of our sample lies within 0.1 mag of our bright and faint limits, where we choose 0.1 mag as a typical amplitude of variability for PMS stars. This number is small enough that we exclude it from further consideration.

2.3. Photometry of High-Mass Stars

In addition to the low-mass members of the λ Ori region, we have also studied the massive stars. In Table 4 we present new Strömgren photometry of one O star and eighteen B stars courtesy of colleagues at the Copenhagen Astronomical Observatory. This table includes all of the stars classified as spectral type O or B0–B5 in the Positions and Proper Motions Catalog (PPM Roeser & Bastian 1988) within 5° of λ Ori, except Bellatrix. We also include all of the PPM B6–B9 stars included in the central 1° . The stars were observed on multiple nights in winter 1998–99 by N. Kaltcheva or in February 2000 by B. Helt. Both data sets were reduced by E. Olsen (see Kaltcheva & Olsen (1999) for details of the observing and reduction procedures).

Notably absent from this list is HD 36862 (or λ Ori B) which was too close to λ Ori A to obtain independent photometry with the 17" aperture of the Copenhagen photometer. On the other hand, we do include HD 245185 which is designated as a B9.5III–V Herbig Ae-Be star by Terranegra et al. (1994). We report their photometry in Table 4 with the others.

3. Massive Stars

Murdin & Penston (1977) obtained high-quality broad band photometry of the 11 OB stars in the center of the star-forming region and used these data to estimate the distance and age of the population. We have improved upon their work by using Strömgren photometry with a larger number of OB stars with more modern models. To accomplish this, we dereddened our Strömgren photometry of the early-type stars and transformed the data to L and T_{eff} . We then compared these quantities to the stellar evolution models of Schaller et al. (1992).

We transformed the calibrated photometry by the following procedure. First we corrected for reddening, using $c_0 = c_1 - 0.20E_{b-y}$, $m_0 = m_1 + 0.32E_{b-y}$ and $E_{b-y} = 0.74E_{B-V}$ (Crawford & Mandwewala 1976), where $E_{b-y} = 0.114 - 0.095c_1 + 1.019(b - y)$, derived from Strom, Strom & Bregman (1971). Using $R_V = 3.1$ we computed A_V values for each star and subtracted these from the observed V values to derive V_o .

Next, we used the dereddened photometry to find T_{eff} using the formulae of Balona (1994). As recommended by that author for stars with $\beta < 2.6$, we used the empirical β/c_0 relation for HD 36822 and HD 36861. All 20 stars had photometry consistent with the “early group” calibrations (i.e. $T_{\text{eff}} > 9500$ K). We also computed the bolometric correction from Balona’s equation and corrected our V_o values to observed m_{bol} .

We then compared the T_{eff} and m_{bol} values to the ZAMS line from the Schaller et al. (1992) $Z = 0.02$ grid. We found that the lower envelope of massive stars matched the main sequence for a distance of 450 pc.

Figure 3 shows the OB stars shifted to 450 pc compared to the Schaller et al. (1992) tracks. In the figure, we differentiate between the central concentration of B stars near λ Ori and others dispersed about the star-forming region. We note that the centrally concentrated stars follow the ZAMS closely, with the exception of the most luminous stars HD 36831 and HD 36822, and HD 36881 at the middle-right of the figure. The dispersed B stars include more photometric non-members. Indeed, all of these could be non-members, since the B-star surface density is similar to the field everywhere in this region except in the center.

In total, eight of the twenty stars are too bright to be consistent with the ZAMS at 450 pc. Among the remaining twelve, the peak-to-peak scatter around the ZAMS corresponds to about a $\pm 15\%$ range in distance. This error is very much larger than the photometric contribution to T_{eff} and m_{bol} errors, so we must assume that the scatter is cosmic. A contribution to this scatter could

arise from internal distance variations in the cluster. If the star-forming region were spherical, the projected diameter implies a depth of $\pm 25\text{--}30$ pc, or up to about $\pm 6\%$ distance error. However, Maddalena & Morris (1987) suggest that the association lies in a flattened face-on ring, so the depth may be smaller. Instead, we suspect that the apparent luminosity spread in these 12 stars is primarily due to multiplicity. The observed 15% spread in apparent distance corresponds to a factor of 1.8 in brightness, just below that expected for equal-mass binaries. In addition, the spread visible in Figure 3 for the twelve near-ZAMS stars resembles the split between single and binary main sequences. This evidence leads us to assume a smaller distance error of $\pm 10\%$. Our final value of 450 ± 50 pc is consistent with the 400 pc distance of Murdin & Penston (1977).

In Figure 3 there are eight stars which do not lie near the ZAMS, even allowing for errors or binarity. For the two hottest of these (which are at the center of the association), we attribute this shift to stellar evolution. That is, for stars as massive as these we can resolve non-zero ages. We classify two others, HD 36267 and 36653, as definite non-members due to their small Hipparcos distances. We cannot so easily explain the other four. Only one of them, HD 36881, is in the center 1° of the star-forming region, where the highest concentration of B stars lies. It is possible that all four are foreground non-members.

The Hipparcos catalog (ESA 1997) contains parallax measurements for 13 of the 20 stars, albeit with relative errors of 25% or larger (Table 5). Five of these stars are located in the central concentration, and give a mean distance of 380 ± 30 pc. The astrometric mean distance is consistent with our photometric distance determination to within the errors in both. The Hipparcos data hint that λ Ori might be significantly closer, but the deviation of the λ Ori measurement from this mean is less than 1σ and only 1.5σ from the derived photometric distance. Because the observed parallax measurements are approaching the uncertainties (i.e., the limit of Hipparcos precision), we are concerned about systematic errors to lower distances (see Lutz & Kelker 1973). Indeed using the Hipparcos distances several stars become underluminous compared to the ZAMS. Thus we choose here to work with our photometric distance of 450 ± 50 pc.

In Table 5 we present E_{B-V} , T_{eff} , L and Hipparcos distances for the 20 OB stars. The luminosity presented assumes a distance of 450 pc.

With a distance modulus in hand, we compared the stars with the model evolution tracks via bilinear interpolation of the L and T_{eff} values in the model grid. While the masses should be well-determined by this interpolation, the ages are highly sensitive to photometric error, particularly near the ZAMS where the age gradient is very steep. Thus we used only the two most massive stars, which are furthest off the ZAMS, to estimate the group age. We find an age of about 5.5 Myr for HD 36861 (λ Ori) and 7.5 Myr for HD 36822.

Table 6 shows the consequences of photometric errors, distance errors and uncertain binarity for the age and mass determination of each star. For HD 36822, the isochrones happen to lie nearly parallel to the luminosity axis, so the age errors are much smaller than the mass errors.

We also tried measuring the luminosity in a distance-independent manner via photometric

measures of $\log g$. Our attempt used the convenient parameterization of Ribas et al. (1997), relating c_0 and β to T_{eff} and $\log g$. However, this technique suffers from large systematics for $T_{\text{eff}} > 25000$ K or $\log g < 4.0$ (I. Ribas 2000, private communication). Since our age determination depends solely on stars hotter than this limit, we had to abandon this approach.

4. Population

4.1. High-Mass Stars

There are a total of 58 PPM stars with spectral type B within 5° of λ Ori. In this region, λ Ori itself is the only PPM O star. In our Strömgren survey, we have observed 19 of these 59, and added one not listed in PPM (HD 245185). If we also include λ Ori B (a B0 star), we count 60 OB stars. Of the 30 late-B PPM stars for which we have no Strömgren photometry, about 5 have PPM magnitudes suggestive of non-membership, given their late-B spectral types. An additional 6 have PPM proper motions which seem too large for membership, however Paper I showed us that unusual proper motions can be interesting. Thus, the 60 OB stars we counted above is an upper limit on the number of OB members in the association.

Our PMS survey fields (shown in Figure 2) contain 16 of these 60 OB stars. Twelve of the 16 are located in Field 6, reflecting the central concentration of the massive stars. We will use these 16 OB stars to compare to the number of low-mass stars in § 5.3 below.

4.2. Low-Mass Stars

4.2.1. Membership

The principal use for our WIYN spectra is to separate the field stars from the PMS stars. As in Paper I, we do this by identifying stars with “strong” lithium absorption, which we define as $W_\lambda(\text{Li}) \geq 0.2\text{\AA}$. Figure 4 justifies this choice by comparing two independent membership diagnostics: lithium and radial velocities. From the figure one can see that the majority of stars with large lithium equivalent width have a narrow radial-velocity dispersion while stars with weak lithium absorption seem to have uncorrelated radial velocities. Our $W_\lambda(\text{Li})$ cutoff was chosen empirically in Paper I, yet it appears to appropriately exclude many stars with velocities inconsistent with association membership just below $W_\lambda(\text{Li}) = 0.2\text{\AA}$.

Worthy of note are the few stars which have velocity just blueward of the main grouping, with $0.1 < W_\lambda(\text{Li}) < 0.2\text{\AA}$ and $10 < V_R < 20$ km s $^{-1}$. These stars have velocities intriguingly similar to the Taurus-Auriga association to the northwest, but their spatial distribution appears random.

Nearly all of the strong lithium stars, on the other hand, have typical Orion velocities: we measure a system mean velocity of 24.5 km s $^{-1}$ by the Gaussian inversion technique, excluding the

double-line binaries marked in Figure 4. By this same method, we measure a velocity dispersion of 2.3 km s^{-1} (or 2.2 km s^{-1} correcting for our 0.57 km s^{-1} measurement error). Gaussian inversion is a much more robust technique than the fitting algorithm we used in Paper I to exclude outliers, so this estimate of the velocity dispersion of the association supersedes previous estimates. Note that many of these strong-lithium velocity outliers could be single-line binary members, but we do not have multiple spectra for any of them, so we cannot address this issue.

4.2.2. *Census*

As enumerated in § 2.2, our lithium criterion identifies 266 stars as PMS members of the association. Neglecting the six stars in the incomplete Fields 1 and 3 leaves 260. Of these, 238 are inside the photometric criteria we used to select stars. Three of the 22 outside the criteria are brighter than $R = 12$ while one is bluer than our isochronal cutoff. The rest of the outliers are fainter stars ($16 < R < 16.5$) which we surveyed with unused WIYN Hydra fibers.

To correct for incompleteness in our spectroscopic survey fields, we use the 96% completeness value computed in § 2.2. We use this value instead of the overall 91.1% completeness since almost none of the PMS stars are found near the blue edge of our photometric selection box, where the completeness is worst. Correcting the 238 observed stars, we find a total PMS population of 248 stars within our selection criteria.

4.2.3. *Comparison to Previous Surveys*

We have taken a very different approach from previous surveys for low-mass PMS stars in the λ Ori region. Our work has emphasized an unbiased survey via lithium absorption in selected spatial regions, while the two previous major surveys have been complete spatial surveys using diagnostics which are biased toward the presence of accretion disks or large stellar activity. Here we compare our young star detection rate to that of the DIL $H\alpha$ survey and the RASS. One should note that while selecting stars to observe spectroscopically in each field of our survey, we were deliberately blind to whether the stars had been previously observed. Thus, the cross-reference rate with these surveys should be similar to our completeness estimated in the end of § 2.2.

The DIL catalog contains 99 objects which at some time had been seen to have $H\alpha$ emission. They detected $H\alpha$ in 82 of those (however, one turned out to be a planetary nebula) and concluded that the other 17 no longer had detectable $H\alpha$ due to variability³. Excluding the PN, we will use 98 as the number of $H\alpha$ stars hereafter. Their survey covered 100 degrees^2 , which include the 8 degrees^2 of our survey. Despite the very different spatial extents of the surveys, 59 of their 98

³DIL claim to have detected 83, but their catalog clearly shows 17 non-detections among the 99 entries. We choose to believe the discrepancy is due to a counting error.

objects lie in one of our 11 survey fields. This large fraction reflects the fact that some of our fields were chosen to trace the dark clouds where DIL found most of their objects. We obtained spectra for 36 of those 59. Of the 22 we missed, 7 are in either of Fields 1 or 3 where we are very incomplete and 13 others are outside of our color-magnitude selection criteria (primarily because they are too bright for our survey). Thus, in our high-completeness fields, we have spectra for 36 of the 39 stars we should have observed: 92% completeness. This is consistent with either the 91.1% or the 96% completeness estimates stated earlier. The three DIL stars we inadvertently missed are DIL 27, 44 and 86.

Among the 36 DIL stars which we observed, 31 show strong lithium absorption and 5 show no detectable lithium. (No weak-lined lithium stars were found.)

For the 31 DIL stars in our sample, comparison of our equivalent width measurement to the $H\alpha$ strength categorization published by DIL showed that the mean $W_\lambda(H\alpha)$ for each DIL category increased as expected, i.e., DIL “Strong” stars have a larger mean $W_\lambda(H\alpha)$ than DIL “Medium” stars, etc. However, the standard deviations of equivalent widths are large. For example, we measure $W_\lambda(H\alpha)$ from 5.8 to 240Å for DIL “Strong” stars. This is likely due to $H\alpha$ variability, as we believe that neither our measurement errors nor any categorization errors made by DIL could be this large. Variability would also explain why DIL missed star 0975-01684382, which has $W_\lambda(H\alpha) = 87\text{Å}$ and clearly stands out in Figure 14.

Of the 5 non-lithium stars, three are labeled by DIL as “Weak” or “Very weak” $H\alpha$ (DIL 31, 48, and 64) while one is “Medium” (DIL 79) and one is “Strong” (DIL 50). We did detect $W_\lambda(H\alpha) = 11\text{Å}$ for DIL 50, but there is no lithium present for that star. For the others, we detected neither lithium absorption nor $H\alpha$ emission. DIL 31 looks like an A star (broad $H\alpha$ absorption) and did not produce a good velocity measurement. The velocities for the others (DIL 48, 50, 64 and 79) are inconsistent with membership, so we can only assume that they are variable- $H\alpha$ non-members.

The RASS has detected a huge number of X-ray sources over the whole sky which have later been confirmed to be PMS stars. The λ Ori region is split between two segments of the RASS follow-up work: the Orion region and the South Taurus region. For Orion, Sterzik et al. (1995) presented a density enhancement of ROSAT X-ray sources in the vicinity of λ Ori. Alcalá et al. (1996), Alcalá, et al. (1998), and Alcalá, et al. (2000) followed up these X-ray sources with photometry and spectroscopy to find 36 PMS stars near λ Ori, seven of which are DIL stars. In Taurus, Neuhäuser, et al. (1995a) announced the RASS detection of PMS candidates. Follow-up data were analyzed by Neuhäuser, et al. (1995b), Neuhäuser, et al. (1995c), Magazzù et al. (1997) and Neuhäuser et al. (1997) to find 10 PMS stars near λ Ori, two of which overlap with the RASS Orion region. Thus, between the two regions, there are 44 PMS stars. Neglecting the seven DIL stars, 6 of the remaining 37 stars lie in one of our survey fields. Of these six, only two had magnitudes faint enough to be in our survey selection criteria. We have spectra for both of these, RXJ0528.9+1046 and RXJ0531.8+1218, and found them to have strong lithium. We also observed two stars which Magazzù et al. (1997) label as non-PMS and found no lithium in these two. Unfortunately the

overlap is so small that our unbiased sample cannot shed light on the biases of X-ray searches, and in particular on the fraction of X-ray quiet PMS stars.

5. PMS Ages and Masses

The strong correlation of radial velocity and lithium equivalent width allows us to confidently conclude that the stars with strong lithium are all members of the star-forming region. This conclusion in turn implies a common distance, which allows us to transform our photometry into mass and age for each star. We perform this transformation by the following procedure, as in Paper I.

5.1. Technique

First, we select a PMS evolutionary model which includes a mapping from L (or g) and T_{eff} to age and mass. In this paper, we will employ the new models of Palla & Stahler (1999, hereafter PS99), which claims to have a more robust definition of zero age than previous models. We also will use the DM98 model (with $Z = 0.02$ and deuterium abundance of 2×10^{-5}) and the extended BCAH98 model (with solar metallicity and variable mixing length) which were discussed in Paper I.

Second, we transform the L , T_{eff} values in the model grid to R and $R-I$. To do this we use Table A5 of Kenyon & Hartmann (1995) to interpolate bolometric correction (BC) and main-sequence $V-R_c$ and $V-I_c$ colors. Using L , BC and $V-R_c$, we compute M_R which we transform to R using a distance modulus for 450 pc. We also redden the isochrones using the extinction of $E_{B-V} = 0.12$ measured for λ Ori by Diplas & Savage (1994). Using $R_V = 3.1$, this corresponds to corrections of $E_{R-I} = 0.097$ and $A_R = 0.27$. Over most of the surveyed region where there is little evidence for molecular gas or extinction, we anticipate that the reddening will be similarly small as toward λ Ori. However, in the regions of B30 and B35 the reddening may be substantially higher. We will elaborate upon results which may be affected by different reddening in the discussion below.

Third, for each PMS star we find in which cell of the model grid it is bounded. This cell is a quadrilateral defined by four nodes, each with age, mass, R , $R-I$ values. Within this cell, we compute the age and mass from the star's R and $R-I$ measurements via bilinear interpolation. If the star's R or $R-I$ values place it outside the limits of the model grid, we extrapolate from the nearest isochrone or isomass segments which bound the star's CMD position.

This procedure differs from most comparisons of stellar data to model tracks in the PMS literature, where the magnitudes are transformed to L , T_{eff} instead of transforming the tracks to the color-magnitude domain. Our technique has the following practical advantages. First, by leaving the stellar data in the color-magnitude domain we avoid the complication of propagating measurement errors into the theoretical plane. Second, we postpone making assumptions about

complications (like binarity and reddening) which our data at present cannot address. Third, for a large number of stars, our technique is computationally simpler since the second step only need to be performed once for each model. This was convenient while we performed tests of how distance and measurement errors affect age and mass computations.

In Figure 5 we show the position of our PMS stars in a color-magnitude diagram. We overlay this diagram with evolutionary tracks and isochrones, in this case the PS99 model. As stated above, our survey criteria limit us to stars with $12 < R < 16$ and a 30 Myr isochrone from D’Antona & Mazzitelli (1994). For the PS99 model at 450 pc, this latter limit lies roughly along a 40–50 Myr isochrone.

As in Paper I, we can see from the CMD that the stars are PMS with ages on the order of 10^6 years. There is a striking lack of PMS stars older than about 10 Myr or younger than about 0.3 Myr. We analyze the age spread and star-formation history in detail in the next section.

Ages and masses derived from the PS99 model are printed in the final columns of Table 2. We do not intend this as an endorsement of this model over the others. Instead, we choose this model because it implies ages and masses between those from the DM98 and BCAH98 models, as demonstrated below.

5.2. Errors and Coevality

The majority of our survey stars have ages in the range of 1–10 Myr. However, this age spread cannot be entirely real. Errors in measurement, binarity, distance and reddening can all contribute to an inflated age spread.

To test the effects of these errors, we tried adjusting our stellar photometry by each of the above sources of error. We sent the resulting $R-I$ and R values through our age/mass calculating pipeline. The results are displayed in Figure 6 in the form of errors in age and mass as a function of error type. For each panel, we display the age and mass of each PMS star, computed in this case from the BCAH98 model. We overlay the limits of the BCAH98 grid with a heavy line. Stars outside this boundary required extrapolation from the grid to compute ages and masses. We note that the BCAH98 is the most limited of the ones with which we have worked. The DM98 and PS99 grids extend to much younger ages and higher masses, so almost no stars are extrapolated with these models. The errors in these other two models are qualitatively very similar to those for the BCAH98 tracks, so we only discuss the latter in detail. Figure 6a shows the effect of varying the $R-I$ magnitudes by ± 0.041 mag, adding the 0.029 R and I errors in quadrature. Ages and masses are much more sensitive to color than magnitude, so the individual R or I errors are not displayed. Figure 6b shows the change caused by varying the distance to 400 pc and 500 pc. Since distance errors do not change the colors, this error is primarily in age, not mass. On the contrary, the reddening errors in Figure 6c hardly change any age estimates. The reddening errors are marked as $E_{B-V} = 0.12 \pm 0.06$. Compared to the variable reddening measured for the massive stars (see

Table 5 where the RMS of E_{B-V} is 0.07) this represents roughly a 1σ spread; it does not of course incorporate larger reddening for stars projected within the dark clouds. Finally we look at the error caused by undetected binaries. Figure 6d shows the age/mass change caused by dividing the R flux by two, simulating an equal-mass binary. Like the distance panel, only the ages are affected significantly, but this correction can only make stars older.

Thus we see that the error in age determination is dominated by uncertainty in distance and binarity, while mass error is affected more by variable reddening and errors in stellar color.

Next we analyze whether photometric errors and undetected binaries can explain the observed spread of ages. To do this, we closely follow the procedure described by Preibisch & Zinnecker (1999). Namely, we have created a simulation of the age spread of a coeval population. For each selected mass point along an isochrone, we calculate the magnitude range above and below a perfect isochrone in which we will find 90% of the stars in the simulation. We then count how many of the actual stars were found in this range. If we find much less than 90% of the observed sample outside of the predicted range, then some of the age spread must be physical.

To compute the predicted age spread, we correct for the brightening due to undetected binaries. We conservatively assume that 100% of the stars are binaries, since this leads to the largest predicted age range. To compute the binary age inflation, we create 30,000 random companions for each primary mass. The mass of each companion is selected from the same mass function as in Preibisch & Zinnecker (1999). Using a set of PMS tracks, we interpolate the R magnitudes of both stars, given their masses, and compute the R magnitude of the composite⁴. The difference between the R magnitude of the primary and that of the binary yields a ΔR . Combining this with photometric and distance errors (0.029 mag and 10%, respectively, at 1σ), we find the ΔR which is greater than that of 90% of the binaries. Thus, for each mass point on a given isochrone we have the expected magnitude deviation from the ideal case. As an example, Figure 7 shows the 90% age range expected for a 5 Myr coeval population using the BCAH98 isochrones. In this calculation we have ignored the error due to variable reddening, since the reddening vector is nearly parallel to the isochrones.

We created coeval models with the DM98, BCAH98 and PS99 isochrones. For each, we adjusted (with 1 Myr steps) the age of the coeval model population until we found a maximum fraction of observed stars falling within the predicted range. For DM98, this maximum occurred at 2 Myr with 58% of the stars. We found a similar maximum at 5 Myr with 53% for BCAH98 and 3 Myr with 52% for PS99. Clearly the best-fit age depends on model choice, but in all cases the fraction of stars was much lower than the 90% expected for coevality. Thus we conclude that our detected low-mass population is not coeval.

⁴Note that our procedure does not take the color difference between the primary and secondary into account. This means that our predicted age spread is slightly underestimated, but our observed age spread is so much larger than the predicted spread that we believe this error is insignificant.

5.3. The Initial Mass Function

We now have masses for both high-mass and low-mass stars in the λ Ori region. From the analysis of the massive stars, we know that stars as massive as $12 M_{\odot}$ have not yet evolved off the main sequence, and indeed λ Ori at $24 M_{\odot}$ is still present in the association. This permits us to easily investigate the initial mass function (IMF) of the star-forming region. In particular, we would like to know if the ratio of high-mass to low-mass stars is consistent with the field IMF. To answer this properly, we must first address our mass biases. The photometric limits of our lithium survey tend to cut diagonally across model evolution isomass lines. Thus, for the extreme masses in our PMS sample, we are only sensitive to a limited range of ages.

Figure 8 shows the PS99-derived ages and masses of our PMS sample bounded by our photometric selection limits transformed into age and mass by the same technique as the stars. Using this figure, we selected a box with edges of constant age or mass which contains a substantial number of stars, yet lies inside our photometric boundary. Such a box is drawn in the figure with age and mass limits of 0.4–8 Myr and 0.4–0.9 M_{\odot} . These limits are chosen subjectively, but this box contains roughly the maximum number of stars. We say this box defines a “bias-free” region, where we are fully sensitive to all ages and masses contained in such a region. We define similar bias-free boxes for other models: for DM98 we use age and mass limits of 0.5–9 Myr and 0.45–0.9 M_{\odot} while we choose 0.5–10 Myr and 0.55–1.2 M_{\odot} for the BCAH98 model. The differences arise from slightly different age and mass scales for the models.

What do these bias-free boxes achieve for us? In the next section, they will allow us to create age histograms which are unaffected by mass biases. Here, they allow us to examine the mass function of an epoch of star formation. Thus, the question stated above is better posed as whether star formation between, say, 0.4 and 8 Myr ago generated the field mass function.

Using the PS99 mass and age limits above, we count 107 low-mass stars to be compared to the 16 OB stars in our survey fields with masses greater than about $2.5 M_{\odot}$ (i.e. B9 or earlier). The Miller & Scalo (1979) (12 Gyr, constant star-formation rate) IMF predicts that given 107 stars in the range of 0.4–0.9 M_{\odot} , we should see 19 OB stars. Following the Monte Carlo procedure from Paper I, we determine that the difference between 16 and 19 is not a significant difference. Thus, the observed ratio of low-mass to high-mass stars is consistent with the field IMF.

The DM98 model predicts 16 OB stars given 72 PMS star, also clearly consistent with the observed number of OB stars. However, the BCAH98 model leads to a rather different conclusion. Within the unbiased BCAH98 age and mass limits of 0.55–1.2 M_{\odot} , we find 161 stars. The field IMF predicts 38 OB stars for this many 0.55–1.2 M_{\odot} stars. This is different from the observed 16 OB stars at the 99.99% confidence level.

We also performed similar tests using the Kroupa, Tout & Gilmore (1993) fit to the field IMF. This approach yielded about half as many predicted OB stars for each of the three PMS models (10, 9 and 21 for PS99, DM98 and BCAH98) compared to the Miller & Scalo predictions. All three

of these represent marginally significant differences from the field

Thus all of the models (with the exception of BCAH98 with Miller & Scalo) suggest that the field IMF has been generated within the fields which we have surveyed. These results differ from Paper I where we found that around the central cluster of OB stars (Field 6) the low-mass stars were under-represented by a factor of two. Evidently including stars outside the center of the association has filled in this apparent deficiency of low-mass stars.

A central question for this research has been whether the formation of the OB stars was joined with a complete IMF either *locally* or *globally*. Paper 1 discussed in detail the issue of whether the IMF local to the OB stars agreed with the field, finding that the factor two deficiency in low-mass stars represented a deviation at a marginal (97.4%) confidence level. The question is further complicated by the fact that kinematic expansion may have removed some low-mass stars from the present vicinity of the OB stars.

The new results from our expanded survey clearly show that the IMF has varied across the star-forming region. If we consider the low- and high-mass populations of all fields outside the central 1° , we find that the low-mass stars are over-represented compared to the Miller & Scalo field IMF by factors of 2, 3 or 7 for DM98, PS99 or BCAH98 respectively, with high statistical significance. Indeed, if we consider only those stars outside our 2° circle, i.e. those stars associated with the clouds B30 and B35, both the BCAH98 and PS99 models indicate that the low-mass stars are over-represented at significant confidence levels; only the DM98 models result in no distinction from the field IMF. The confidence of these conclusions is only enhanced if any of the OB stars are not association members.

Thus we see that neither the outer nor the inner region of the λ Ori association creates the field IMF by itself. The inner region is marginally over-populated by OB stars while the outer region is significantly over-populated by low-mass stars. Only when the entire spatial extent of our survey is considered do we find a ratio similar to the field, and then only in the cases of the DM98 or PS99 models. Thus the *global IMF* in our surveyed region resembles the field while the *local IMF* appears to vary substantially across the star-forming region.

6. Spatial Distribution

6.1. Low-Mass Stellar Surface Density

The λ Ori region is ideal for investigation of the impact of massive stars on low-mass star formation because the central concentration of the most luminous stars allows for simple parameterization of the properties of the low-mass stars as a function of radius. In the following discussion, we define radius as the projected angular distance from λ Ori. The pattern of target fields makes for an irregularly shaped distribution of area surveyed as a function of radius, which we have computed for the purposes of surface density measurements. We also exclude fields 1 and 3 which have been

very incompletely surveyed.

In Figure 9 we show the surface density of PMS stars (solid line) and OB stars (dashed line) as a function of radius. Comparing the PMS star density distribution to a control sample of the survey stars with no detectable lithium, we find with a Kolmogorov-Smirnov (K-S) test that the strong lithium stars are inconsistent with a uniform distribution with a high degree of confidence. Even excluding the obvious concentration within 1° , the excess of strong lithium stars near a radius of 2.4° has only a 1% chance of being a random excursion from the control distribution. Notably, the excess at 2.4° coincides with the fronts of both dark clouds B30 and B35 (in fields 2 and 9) where the DIL survey found a large number of $H\alpha$ stars. One can see this higher density on the cloud faces in Fields 2 and 9 in Figure 2.

Thus, there are at least three enhancements in the density of low-mass stars. One corresponds to the central concentration of OB stars while the other two lie at the fronts of the two molecular clouds B30 and B35. A more uniformly distributed but less dense population fills the space in between. These three enhancements echo the findings of Gomez & Lada (1998), who found similar enhancements considering only the OB stars and DIL $H\alpha$ sources. We now see that the OB and $H\alpha$ surface-density enhancements were highlighted regions of a much larger complex of low-mass star formation.

6.2. Age

To examine the spatial dependence of the star formation history, we divide the PMS sample into two samples divided at 2° from λ Ori, as shown in Figure 2. The “center” subsample consists of stars lying inside of the molecular ring; half of these stars lie within 0.5° of λ Ori (Paper I). The “cloud” subsample consists primarily of projected on or near B30 and B35. Some “cloud” stars likely experience higher reddening than stars in the “center” sample, but their derived age distribution will not be seriously affected as a result of the alignment of isochrones with the reddening vector (§ 5.2).

For each of these two subsamples, Figures 10 (DM98), 11 (PS99) and 12 (BCAH98) show the star formation rate as a function of the age computed by comparison with a given model. (Note that the small completeness corrections of Table 3 have been applied.) As expected, the different models produce different absolute age scales. More importantly, all three stellar evolution models produce pronounced differences between the “center” and “cloud” age distributions. A K-S test reports that the probability of the two distributions arising from the same parent population is about less than 10^{-4} for all three models. On the other hand, we find no significant age distribution differences between the two sides of the “cloud” population (i.e. the stars near B35 versus those near B30).

To address issues of age bias we present a much more conservative comparison in Figure 13. This figure is identical to Figure 12 except that we include only stars which fall in regions where our survey is complete in age/mass space, as discussed in § 5.3. The error bars in this figure represent

the square root of the number of stars per bin before area or rate corrections were made. While the K-S probability statistic decreases to 6×10^{-6} (due in part to the loss of half the stars), the difference is still pronounced. For this conservative approach to the DM98 and PS99 versions of the age comparison (not shown), we find much weaker K-S confidences of 0.4 and 3×10^{-4} respectively. The DM98 result is exceptionally weak because the chosen age and mass constraints miss most of the PMS stars because the DM98 models imply much lower ages and masses than the other models. If we instead choose a bias-free box more appropriate to this model, namely 0.3–3 Myr and 0.3–0.7 M_{\odot} (emphasizing the greater number of younger, lower-mass stars), we find a significant difference: K-S probability of 2×10^{-3} . Thus, our conclusion of distinct age differences is secure.

We note another possible bias linked to reddening. If the youngest stars found in the B30 and B35 clouds are more embedded in the clouds and thus more heavily reddened, the effect will be to preferentially remove them from our sample since the mass function will insure that reddening moves more of them below our faint magnitude limit than will be added at our bright magnitude limit. Thus the youngest age bins may somewhat underrepresent the most recent star-formation rate in the B30 and B35 clouds.

Consideration of these biases does not change the essential conclusion: the star formation history in the vicinity of the central OB stars differs significantly from the star formation histories of the B30 and B35 clouds. This conclusion is independent of stellar evolution model.

The qualitative star-formation story also does not depend on model. Specifically, star formation commenced throughout the region at a slow rate. In the subsequent few Myr, the star formation rate increased dramatically everywhere, but fastest in the center region. Remarkably, K-S tests show that the early star formation history is indistinguishable between the central region, the B30 cloud, and the B35 cloud.

Recently, the low-mass star formation rate declined sharply in the center while it continued to climb near the clouds. At the present day, star formation appears to have all but ceased in the center while the cloud region still appears to be bearing stars.

The quantitative timeline of the star formation depends on stellar evolution model. In the context of the BCAH98 model, star formation began everywhere 8–10 Myr ago and the central star formation slowed 2 Myr ago. With the DM98 model star formation began only 4 Myr ago and just within the last 1 Myr has the central star formation slowed. The PS99 model provides an intermediate timeline.

The choice of timeline is significant, because the derived ages for the two luminous stars HD 38361 and HD 36822 are fixed benchmarks against which the low-mass stellar ages change with model. Thus in Paper 1 we considered two scenarios for the region, one in which the low- and high-mass stars formed coevally (BCAH98 models) and one where the low-mass stars formed in a burst (DM98 models) triggered by a supernova.

In Paper 1 we expressed concern that the DM98 models indicated ongoing star formation

within the last Myr in the central region despite the present absence of natal gas there. That implausibility leads us to prefer the PS99 or BCAH98 models, which we will use for the remainder of this paper. Nonetheless, we caution that for all models derived ages of less than 1 Myr, and quantitative conclusions drawn from those ages, are not yet secure.

6.3. Balmer Emission

A principal result of Paper I was the surprising lack of H α emission for young stars cospatial with the massive stars. Of the 72 PMS stars found in the central region, only 2 showed strong H α emission. Here we analyze the spatial distribution of H α emission strength across the extent of the star-forming region.

Figure 14 shows the strength of stellar H α emission⁵ for strong lithium stars as a function of distance from λ Ori. The abscissa has been modified by assigning a negative value to radii east of λ Ori and positive values to the west, thus dividing the distribution into the B35 side (east) and the B30 side (west) of the star-forming region. This figure also identifies which stars have matches in the DIL catalog (marked as open circles).

Despite our higher sensitivity to H α emission, our observations do not alter the findings of DIL. In Figure 14 most of the strong H α stars appear at about 2.4° radius from λ Ori. Echoing the stellar density enhancements shown in Figure 9, the H α stars cluster along the inward-facing edges of the B30 and B35 clouds. The essential new insight is that these clustered H α stars are not in fact isolated instances of star formation, but rather are part of a larger local population of PMS stars, all of which are immersed in a more distributed, lower-density PMS stellar population.

Given that both the youngest stars and the H α emission stars are only found in the vicinity of the B30 and B35 clouds, a linkage between H α emission and age might be expected. In fact, our data show a weak correlation. We have compared the distributions of ages for two samples: one with $W_\lambda(\text{H}\alpha) > 10\text{\AA}$ and one with $W_\lambda(\text{H}\alpha) < 10\text{\AA}$. The K-S probability that they arise from a single parent distribution is about 0.05, marginally significant.

This somewhat younger age distribution of the H α stars is also seen in other star forming regions, where the age distributions of H α stars and weak-lined stars differ but overlap. More significant here is the fact that many of the H α stars associated with B30 and B35 have ages similar to PMS stars found in the central region. And yet almost none of the stars in the central region show H α emission. A similar point was made in Paper I by comparing the central PMS stellar population with the Taurus-Auriga population. It would appear that the absence of H α emission from very young stars in the central region strongly suggests an environmental influence,

⁵The H α equivalent width data has been corrected for normal chromospheric Balmer emission/absorption by fitting a line to our $W_\lambda(\text{H}\alpha)$ versus $R - I$ relation. The resulting empirical function $6.9 \times (R - I) - 4.5\text{\AA}$ is subtracted from the measured H α equivalent width for each star. The maximum correction is about 8\AA .

likely related to the luminous OB stars.

7. Star Formation History of the λ Ori Region: The Supernova Hypothesis

Our lithium-based survey for PMS stars in the λ Ori star forming region has revealed 266 PMS stars, with half of the stars concentrated in one of three density enhancements: near B35, near λ Ori, and near B30. Figure 15 shows the spatial distribution of these PMS stars, compared to IRAS 60 μ m emission in which the dark clouds are evident.

Using the ages of these stars, we have traced the star-formation history of the region. We found that star formation commenced some 8–10 Myr ago and has since been accelerating, with the notable exception of an abrupt decline in the central region of the association 1–2 Myr ago. In addition, a CO survey clearly shows that the central region of the association has been largely vacated of molecular gas. Evidently something happened 1–2 Myr ago that dramatically changed the star-forming region. In Paper I we described how a supernova explosion could explain many properties of the central region around λ Ori. Here we restate and elaborate the scenario in the context of our expanded survey.

DIL suggested that the H α stars were a fossil remnant tracing the original molecular cloud. We begin from a similar starting point, postulating a giant molecular cloud extending from the present locations of B30 through λ Ori to B35. The B30 and B35 clouds (possibly much more massive) existed as part of this giant molecular cloud, accompanied by a massive cloud core near where we find the OB stars concentrated today. (Whether the molecular cloud was in fact limited to such a linear spatial distribution is not clear, and will become more evident when our survey for PMS stars is extended to regions within the molecular ring along a diameter perpendicular to the one of this study.)

Roughly 8–10 Myr ago, star formation began in the cloud. Both high- and low-mass stars were formed in the massive cloud core, including one or more now-vanished 30–40 M_{\odot} O stars. Low-mass stars also formed elsewhere in the molecular cloud, possibly accompanied by a few isolated B stars. Distributed star formation likely also occurred, but the star formation rates were highest in the cloud core and the B30 and B35 clouds.

Until 1–2 Myr ago, the star formation rate increased continuously everywhere. In the cloud core this acceleration in star formation rate may have had a causal connection to gas compression from OB star winds. However, the central OB stars cannot explain the increased star formation rate elsewhere, or the similarities of the star formation histories throughout the region prior to 1–2 Myr ago. Kinematic arguments made in Paper I require that the stellar population of the cloud core remain bound by the parent cloud until roughly 1 Myr ago, lest the OB stars have dispersed by the present time. The strong contrast of this 1 Myr dynamical age to the 6–7 Myr stellar evolution age of the massive stars supports the scenario where the OB winds and radiation were not enough to disperse the cloud without a supernova. The survival of the cloud core until such a late date

would also imply that the OB stars could not have caused the increased star formation rate also seen in the B30 and B35 clouds, since the core would have obstructed any influence the massive stars could have at that distance. Given a sound speed in cold molecular gas of less than 1 km/sec, this apparent synchronization of star formation is not easily explained.

During this time as a bound system in the cloud core, many of the orbiting PMS stars would have had close interactions with the luminous OB stars. We suggest that the consequential photodissociation of their circumstellar disks is the explanation for the lack of present H α emission indicative of accretion disks.

Roughly 1–2 Myr ago, one or more of the postulated massive O stars exploded as supernovae. The resulting shock wave dispersed the gas in the cloud core, terminating star formation in that region and unbinding the stars. The subsequent free expansion has not yet dispersed the OB stars. Nonetheless, with a velocity dispersion of about 2 km s $^{-1}$ (Paper 1) some expansion has occurred, implying that the initial stellar density of both the OB stars and the central low-mass stars was likely much higher prior to the supernova explosion. The region may have been similar to the Trapezium cluster, albeit with substantially less stellar mass.

Presumably the shock wave also contributed to the dispersal of much of the rest of the giant molecular cloud and the formation of the present molecular ring and H I arc (Zhang & Green (1991)). However, the relative contributions of the supernova shock, the subsequent ionization front, and stellar winds remain to be explored. Possibly the disks of existing PMS stars were also damaged by the supernova blast, further reducing accretion onto these stars.

Evidently the supernova was not able to terminate the star formation in the B30 and B35 clouds. Instead the B30 and B35 clouds are only now being dissociated by the OB stars to reveal numerous formerly-embedded young stars. The stars distributed near the inward cloud faces (Figure 15) may trace the former extent of these clouds. We would expect that in another Myr these faces of the clouds will be further eroded, revealing more PMS stars. In fact, Mathieu et al. (1990) find that there are numerous IRAS sources with the colors of young stellar objects projected within the B30 cloud. B35 on the other hand does not show embedded sources, which is somewhat surprising given the presence of PMS stars near the stellar birthline. It would appear that star formation in B35 has recently ended.

Given ionization fronts, massive star stellar winds, and a conjectured supernova, one might expect triggered or sequential star formation to be part of this story. Indeed, the very young stars at the cloud faces might be taken as evidence for compression-induced star formation. However, these very young stars are interspersed (in projection) amidst stars with ages ranging from 2 Myr to 10 Myr, and so it is not clear that they have a distinct origin. Interestingly, the BCAH98 age distribution shows a rapid increase in star formation rate at the clouds shortly after the central star formation rate drops, as might be expected given an outgoing shock wave. However, this morphology is unique to the BCAH98 age distribution and we are hesitant to give it much weight.

Thus we find little evidence in the age and spatial distributions for triggered sequential star

formation. Indeed, the accelerating star formation seen in the B30 and B35 clouds is typical of star forming regions, according to Palla & Stahler (2000). While the cessation of star formation in the λ Ori region is evidently linked to the action of massive stars, the process initiating star formation remains unclear.

Note that the association of 2–10 Myr stars with the present B30 and B35 clouds would suggest that the clouds have not moved far on that timescale. In contrast to the models of Maddalena & Morris (1987), if our scenario is correct the massive stars were trapped in the central core too long to impart much momentum to the distant clouds.

Finally, we remind the reader that the star formation history of the entire λ Ori region has already generated enough low-mass stars to reproduce the field IMF. However we have seen that in any one location the local IMF can have a substantially different shape. In particular, the OB stars are over-represented in the center while they are balanced by excess low-mass stars born tens of parsecs away.

8. Summary

An expansion of our photometric and spectroscopic lithium-based survey for PMS stars in the λ Ori star-forming region has revealed 266 PMS stars over 8 degrees², allowing a detailed study of the star-formation history of the association. The placement of our survey fields gives us a sample of young low-mass stars crossing a diameter of the star-forming region. The surface density of these stars shows a large enhancement in the center of the association associated with the OB stars. Regions of high stellar density also exist on the inward faces of both the B30 and B35 dark clouds. Finally, a low surface-density distributed population is present.

New Strömgren photometry of the OB stars allows an independent distance and age estimate for the OB association. The B-star main sequence provides a distance of 450 ± 50 pc, while two turn-off stars indicate an age of 6–7 Myr for the OB stars. Using this distance, we compute ages and masses for all the low-mass stars by comparing their photometry to theoretical evolutionary tracks. Three different models give different stellar properties, but all three indicate that star formation started slowly and then increased in rate over the entire region. Recently, the stellar birth rate in the center of the association plummeted while stars continue to be born near B30 and B35. Using the BCAH98 model to provide a quantitative timeline, star formation began 8–10 Myr ago, roughly coevally with the massive stars, and the central star formation ceased 1–2 Myr ago.

We construe from the age distributions and the spatial morphology of the young population that a supernova event 1–2 Myrs ago disrupted the massive cloud core in which λ Ori and neighbors were formed. This supernova terminated the birth of stars in the vicinity of the OB stars, and exposed the B30 and B35 clouds to erosive conditions, now exposing young stars. The central association (including the OB stars and neighboring low-mass stars) is now locally unbound and in the process of dissipating into the galactic field. The stars in the vicinity of the B30 and B35 clouds

will enter the field with the dissipation of those clouds. The union of star formation throughout the entire region may match the IMF derived from field stars (depending on stellar evolution model).

Remarkably almost all of the young PMS stars in the vicinity of the OB stars are devoid of $H\alpha$ emission, indicating an absence of accretion disks. Many $H\alpha$ emission stars have been found near the B30 and B35 clouds, 20 pc distant from λ Ori. Stellar age alone cannot explain this difference, and we attribute the paucity of accretion disks to photoevaporation from the OB stars and perhaps to the supernova event. Infrared studies of these stars to search for evidence of disk material would be well merited.

From these results in combination with Paper I we draw the following conclusions:

1. With multi-object spectroscopy, the combination of lithium line absorption and radial velocity proves to be a very powerful diagnostic for identification of low-mass PMS stars. When combined with multi-color photometry hundreds of PMS stars can be sifted from many tens of thousands of field stars. Unlike $H\alpha$ and X-ray surveys, this diagnostic is not heavily biased toward specific types of PMS stars.
2. The λ Ori region clearly shows that OB stars terminate star formation via molecular cloud dispersal, although the specific mechanism for the dispersal is not certain. The termination has been incomplete at distances of 20 pc from the OB stars where molecular clouds have survived and continue to generate stars.
3. Despite ionization fronts, massive star winds, and a conjectured supernova, we have not found evidence in the age or spatial distributions for triggered or sequential star formation.
4. The local IMF varies across the star-forming region. Depending on choice of stellar evolutionary model, the identified young stellar population in the entire surveyed region may replicate the field IMF.

Scaling the field IMF by the number of OB and low-mass stars in our surveyed region, we compute a lower-limit for the total stellar mass of $305 M_{\odot}$ for stars above $0.1 M_{\odot}$. While more of the region remains to be surveyed, clearly the contribution of stellar mass to the field will be modest. In addition, the region will not contribute any star clusters to the galactic population. As such, the λ Ori region may be a model for the star-formation process in moderate-mass molecular clouds.

CJD acknowledges continued support from the NASA National Space Grant College and Fellowship Program through the Wisconsin Space Grant Consortium. This work is supported by NSF grant AST 94-1715 and NASA ADP grant NRA-98-03-ADP-003.

A. The DIL stars

In our study of the λ Ori star-forming region, we have invested much time working with the DIL catalog of $H\alpha$ stars. In Table 7 we present follow-up data and notes we have compiled for these stars. Here we present details of how these data were generated.

In our work with the lithium PMS sample, we encountered difficulty cross-referencing with the DIL stars. Many of the coordinates published in the DIL catalog are adequate, but it turns out that several have large errors. To positively identify the stars, we have used the finding charts from DIL and their referenced works: Joy (1949), Haro, Iriarte & Chavira (1953) and Manova (1959). We compared the positions of the stars on these charts to the Digitized Sky Survey and retrieved coordinates via a modified version of the XSpam tool developed at the STScI. We then matched these coordinates with the appropriate USNO-A1.0 source, checking that slight coordinate differences did not cause us to choose the wrong star. When the USNO-A2.0 database later became available, we performed coordinate searches to match the A1.0 IDs to those from the A2.0 catalog. Finally, to cross-reference with our lithium survey, we simply matched USNO A2.0 IDs.

REFERENCES

- Alcalá, J. M., Chavarría-K., C. & Terranegra, L. 1998, *A&A*, 330, 1017
- Alcalá, J. M., Covino, E., Torres, G., Sterzik, M. F., Pfeiffer, M. J. & Neuhäuser, R. 2000, *A&A*, 353, 186
- Alcalá, J. M., Terranegra, L., Wichmann, R., Chavarría-K., C., Krautter, J., Schmitt, J. H. M. M., Moreno-Corral, M. A., De Lara, E. & Wagner, R. M. 1996, *A&AS*, 119, 7
- Balona, L. A. 1994, *MNRAS*, 268, 119
- Baraffe, I., Chabrier, G., Allard, F. & Hauschildt, P. H. 1998, *A&A*, 337, 403
- Briceño, C., Hartmann, L. W., Stauffer, J. R., Gagne, M., & Stern, R. A. 1997, *AJ*, 113, 740
- Crawford, D. L. & Mandwewala, N. 1976, *PASP*, 88, 917
- D’Antona, F. & Mazzitelli, I. 1994, *ApJS*, 90, 467
- D’Antona, F. & Mazzitelli, I. 1997, *Memorie della Societa Astronomica Italiana*, 68, 807
- D’Antona, F. & Mazzitelli, I. 1998, *ASP Conf. Ser. 134: Brown Dwarfs and Extrasolar Planets*, 442
- Diplas, A. & Savage, B. D. 1994, *ApJS*, 93, 211
- Dolan, C. J. & Mathieu, R. D. 1999, *AJ*, 118, 2409 (Paper I)
- Duerr, R., Imhoff, C. L. & Lada, C. J. 1982, *ApJ*, 261, 135
- ESA, 1997, *The Hipparcos Catalog*, ESA SP-1200
- Feigelson, E. D. 1996, *ApJ*, 468, 306
- Gomez, M. & Lada, C. J. 1998, *AJ*, 115, 1524
- Guillout, P., Sterzik, M. F., Schmitt, J. H. M. M., Motch, C., Egret, D., Voges, W. & Neuhäuser, R. 1998, *A&A*, 334, 540
- Haro, G., Iriarte, B. & Chavira, E. 1953, *Boletin de los Observatorios Tonantzintla y Tacubaya*, 1, 3
- Hillenbrand, L. A. 1997, *AJ*, 113, 1733
- Joy, A. H. 1949, *ApJ*, 110, 424
- Kaltcheva, N. T. & Olsen, E. H. 1999, *A&A*, 352, 600
- Kenyon, S. J. & Hartmann, L. 1995, *ApJS*, 101, 117

- Kroupa, P., Tout, C. A. & Gilmore, G. 1993, MNRAS, 262, 545
- Landolt, A. U. 1983, AJ, 88, 439
- Landolt, A. U. 1992, AJ, 104, 340
- Lang, W. J. & Masheder, M. R. W. 1998, PASA, 15, 70
- Lutz, T. E. & Kelker, D. H. 1973, PASP, 85, 573
- Lutz, T. E. & Uppgren, A. R. 1980, AJ, 85, 1390
- Maddalena, R. J. & Morris, M. 1987, ApJ, 323, 179
- Magazzù, A., Martín, E. L., Sterzik, M. F., Neuhäuser, R., Covino, E. & Alcalá, J. M. 1997, A&AS, 124, 449
- Manova, G. A. 1959, Soviet Astronomy, 3, 188
- Mathieu, R. D., Margulis, M., Sofia, U. J., & Marschall, L. A. 1990, unpublished
- McGlynn, T., Scollick, K., White, N., 1998, IAU Symposia, 179, 465
- Miller, G. E. & Scalo, J. M. 1979, ApJS, 41, 513
- Monet, D., Bird, A., Canzian, B., Harris, H., Reid, N., Rhodes, A., Sell, S., Ables, H., Dahn, C., Guetter, H., Henden, A., Leggett, S., Levison, H., Luginbuhl, C., Martini, J., Monet, A., Pier, J., Riepe, B., Stone, R., Vrba, F., Walker, R. 1996, USNO-A1.0, (U.S. Naval Observatory, Washington DC)
- Murdin, P. & Penston, M. V. 1977, MNRAS, 181, 657
- Neuhäuser, R., Sterzik, M. F., Schmitt, J. H. M. M., Wichmann, R. & Krautter, J. 1995a, A&A, 295, L5
- Neuhäuser, R., Sterzik, M. F., Schmitt, J. H. M. M., Wichmann, R. & Krautter, J. 1995b, A&A, 297, 391
- Neuhäuser, R., Sterzik, M. F., Torres, G. & Martín, E. L. 1995c, A&A, 299, L13
- Neuhäuser, R., Torres, G., Sterzik, M. F., & Randich, S. 1997, A&A, 325, 647
- Palla, F. & Stahler, S. W. 1999, ApJ, 525, 772
- Palla, F. & Stahler, S. W. 2000, ApJ, in press
- Preibisch, T. & Zinnecker, H. 1999, AJ, 117, 2381
- Ribas, I., Jordi, C., Torra, J. & Giménez, A. 1997, A&A, 327, 207

- Roeser S. & Bastian U. 1988, A&AS, 74, 449
- Schaller, G., Schaerer, D., Meynet, G. & Maeder, A. 1992, A&AS, 96, 269
- Sterzik, M. F., Alcalá, J. M., Neuhäuser, R. & Schmitt, J. H. M. M. 1995, A&A, 297, 418
- Strom, S. E., Strom, K. M. & Bregman, J. N. 1971, PASP, 83, 768
- Terranegra, L., Chavarría-K., C., Diaz, S. & González-Patiño, D. 1994, A&AS, 104, 557
- van Altena, W. F., Lee, J. T., Lee, J.-F., Lu, P. K. & Upgren, A. R. 1988, AJ, 95, 1744
- Wichmann, R., Krautter, J., Covino, E., Alcalá, J. M., Neuhäuser, R. and Schmitt, J. H. M. M. 1997, A&A, 320, 185
- Zhang, C. Y. & Green, D. A. 1991, AJ, 101, 1006

Table 1. Improved Data for Paper I Stars

ID	ID	USNO-A2.0 Coordinates		V	V-R	R-I	log Age ^a	Mass ^a
lOri	lOri	R.A.	Decl				yr	M_{\odot}
1	J053347.2+095539	05 33 47.220	09 55 38.69	14.16	0.82	0.83	6.35	0.86
2	J053349.9+095038	05 33 49.864	09 50 38.18	16.03	0.98	1.11	6.51	0.49
3	J053351.7+093822	05 33 51.723	09 38 21.54	14.63	0.89	0.92	6.29	0.69
4	J053356.3+095357	05 33 56.347	09 53 57.07	15.69	1.20	1.36	5.76	0.34
5	J053402.0+094106	05 34 02.027	09 41 06.24	13.39	0.70	0.65	6.44	1.32
6	J053405.0+095704	05 34 04.966	09 57 04.01	16.06	1.01	1.10	6.52	0.49
7	J053405.6+094247	05 34 05.572	09 42 46.76	12.75	0.59	0.55	6.69	1.55
8	J053413.7+092920	05 34 13.712	09 29 20.01	13.57	0.61	0.58	6.81	1.26
9	J053432.8+095930	05 34 32.755	09 59 29.92	14.21	0.75	0.69	6.77	1.08
10	J053435.2+092749	05 34 35.168	09 27 49.22	16.91	1.14	1.40	6.30	0.33
11	J053435.6+095944	05 34 35.618	09 59 43.64	16.42	1.17	1.32	6.24	0.36
12	J053436.2+095344	05 34 36.212	09 53 44.37	15.91	1.14	1.24	6.20	0.39
13	J053437.8+093153	05 34 37.794	09 31 52.99	15.44	0.91	0.90	6.79	0.73
14	J053439.2+095255	05 34 39.199	09 52 55.13	15.09	0.92	0.86	6.73	0.79
15	J053439.7+094146	05 34 39.702	09 41 45.86	15.85	1.03	0.94	6.82	0.68
16	J053439.8+100622	05 34 39.788	10 06 22.17	16.08	1.06	1.16	6.36	0.44
17	J053442.5+101154	05 34 42.475	10 11 54.31	13.53	0.78	0.72	6.30	1.16
18	J053447.2+100243	05 34 47.245	10 02 42.90	14.01	0.76	0.74	6.55	1.05
19	J053448.5+095716	05 34 48.455	09 57 15.91	15.79	1.01	1.06	6.49	0.53
20	J053449.0+095802	05 34 49.007	09 58 02.24	16.27	1.16	1.32	6.20	0.36
21	J053449.9+094101	05 34 49.930	09 41 01.00	14.54	0.86	0.84	6.51	0.82
22	J053450.4+095148	05 34 50.440	09 51 47.60	15.58	0.88	0.95	6.72	0.65
23	J053453.7+092657	05 34 53.731	09 26 57.01	15.82	0.97	0.93	6.85	0.69
24	J053506.0+100020	05 35 06.035	10 00 19.60	12.77	0.53	0.49	7.02	1.31
25	J053507.0+094858	05 35 06.951	09 48 57.75	15.40	0.97	0.95	6.58	0.66
26	J053508.3+094254	05 35 08.346	09 42 54.11	12.92	0.59	0.53	6.82	1.44
27	J053509.0+092660	05 35 09.042	09 26 59.69	16.38	1.16	1.34	6.21	0.35
28	J053509.6+093209	05 35 09.552	09 32 09.49	14.07	0.69	0.65	6.80	1.13
29	J053515.1+100107	05 35 15.134	10 01 06.83	16.76	1.25	1.42	6.21	0.32
30	J053517.2+095112	05 35 17.158	09 51 11.77	16.46	1.14	1.16	6.53	0.44
31	J053517.7+092345	05 35 17.697	09 23 44.67	13.49	0.69	0.63	6.53	1.30
32	J053518.4+100238	05 35 18.421	10 02 38.44	16.73	1.02	1.22	6.62	0.40
33	J053519.9+100237	05 35 19.923	10 02 36.94	16.18	1.11	1.17	6.36	0.43
34	J053521.5+094410	05 35 21.489	09 44 10.43	16.80	1.12	1.30	6.44	0.37
35	J053522.2+095228	05 35 22.197	09 52 27.62	15.43	0.95	0.87	6.85	0.77
36	J053525.4+100838	05 35 25.378	10 08 38.42	16.21	1.17	1.33	6.17	0.35
37	J053529.0+093521	05 35 28.984	09 35 21.04	14.81	0.81	0.69	7.06	0.97

Table 1—Continued

ID	ID	USNO-A2.0 Coordinates		V	V-R	R-I	log Age ^a	Mass ^a
lOri	lOri	R.A.	Decl				yr	M_{\odot}
38	J053530.5+095034	05 35 30.467	09 50 34.07	17.22	1.35	1.64	6.00	0.24
39	J053534.8+100036	05 35 34.814	10 00 35.78	15.87	1.07	1.19	6.24	0.41
40	J053535.7+094436	05 35 35.730	09 44 35.53	17.23	1.22	1.35	6.53	0.35
41	J053539.5+095033	05 35 39.478	09 50 33.10	16.76	1.22	1.49	6.07	0.30
42	J053548.6+101912	05 35 48.621	10 19 12.33	16.77	1.12	1.29	6.44	0.37
43	J053549.4+093818	05 35 49.353	09 38 18.22	15.97	1.01	1.07	6.57	0.53
44	J053551.3+095511	05 35 51.314	09 55 11.11	15.69	1.05	1.19	6.20	0.42
45	J053554.3+100424	05 35 54.349	10 04 23.63	12.89	0.61	0.59	6.38	1.54
46	J053555.4+095631	05 35 55.434	09 56 31.13	14.43	0.93	0.93	6.06	0.66
47	J053555.7+095053	05 35 55.670	09 50 53.23	17.41	1.33	1.67	6.05	0.23
48	J053555.8+095622	05 35 55.838	09 56 21.91	16.85	1.16	1.30	6.45	0.37
49	J053557.1+094653	05 35 57.072	09 46 52.71	16.79	1.16	1.45	6.21	0.31
50	J053557.7+094734	05 35 57.668	09 47 34.20	15.68	1.03	1.10	6.30	0.49
51	J053557.9+095434	05 35 57.930	09 54 33.58	14.86	0.94	0.97	6.21	0.60
52	J053559.6+092724	05 35 59.556	09 27 24.21	13.87	0.52	0.51	7.52	0.96
53	J053602.9+094208	05 36 02.874	09 42 07.61	15.22	0.92	0.91	6.64	0.71
54	J053607.1+100948	05 36 07.112	10 09 47.74	16.78	1.15	1.37	6.29	0.34
55	J053609.3+094703	05 36 09.300	09 47 02.71	16.46	1.13	1.39	6.20	0.33
56	J053616.6+095048	05 36 16.618	09 50 48.50	15.31	0.94	1.01	6.36	0.57
57	J053618.6+094509	05 36 18.584	09 45 09.17	13.26	0.57	0.55	7.00	1.26
58	J053619.0+100351	05 36 19.046	10 03 50.97	14.87	0.89	0.88	6.55	0.75
59	J053620.2+094402	05 36 20.225	09 44 02.14	15.19	0.99	1.08	6.16	0.51
60	J053620.5+095219	05 36 20.511	09 52 18.95	15.04	0.87	0.84	6.78	0.82
61	J053626.3+095114	05 36 26.331	09 51 14.09	16.31	1.02	1.10	6.66	0.49
62	J053628.9+095427	05 36 28.912	09 54 27.16	16.57	1.11	1.26	6.39	0.38
63	J053638.1+094051	05 36 38.056	09 40 50.96	13.77	0.74	0.69	6.51	1.16
64	J053638.6+093506	05 36 38.621	09 35 05.56	16.03	1.09	1.27	6.21	0.38
65	J053647.1+100552	05 36 47.103	10 05 52.05	15.74	0.98	1.01	6.59	0.58
66	J053652.1+093403	05 36 52.097	09 34 03.08	13.17	0.68	0.69	6.23	1.24
67	J053652.6+095257	05 36 52.645	09 52 56.59	16.69	1.19	1.44	6.19	0.32
68	J053653.1+094156	05 36 53.086	09 41 55.87	13.76	0.70	0.66	6.56	1.18
69	J053654.9+095025	05 36 54.867	09 50 25.13	15.54	0.97	0.94	6.70	0.68
70	J053657.5+095326	05 36 57.499	09 53 25.89	16.05	1.03	1.11	6.48	0.48
71	J053710.2+095527	05 37 10.172	09 55 27.10	16.72	1.08	1.34	6.34	0.35
72	J053725.4+095345	05 37 25.354	09 53 45.02	16.45	1.21	1.47	5.96	0.30

^aAges and masses are interpolated from the Palla & Stahler (1999) stellar evolution models.^bThis star does not exist in the USNO-A2.0 database. The coordinates (A1.0) and magnitudes listed are from Paper I.

Table 2. Pre-main-sequence Stellar Data

ID	ID	USNO-A2.0	Coordinates	V	V-R	R-I	$W_{\lambda}(\text{Li})^a$	$W_{\lambda}(\text{H}\alpha)^a$	V_r	$\log \text{Age}^b$	Mass^b
IOr	IOr	R.A.	Decl				\AA	\AA	km s^{-1}	yr	M_{\odot}
73	J052533.7+113849	05 25 33.683	11 38 49.01	15.47	1.05	0.99	0.44	0.17	-0.82	6.46	0.60
74	J052541.4+114215	05 25 41.434	11 42 15.32	15.50	0.90	0.80	0.27	-5.30	11.10	7.11	0.83
75	J052549.7+115226	05 25 49.726	11 52 25.75	16.42	0.90	0.79	0.36	2.90	23.72	7.71	0.65
76	J052556.5+105451	05 25 56.488	10 54 50.82	13.53	0.66	0.64	0.45	0.75	25.48	6.53	1.28
77	J052606.6+105741	05 26 06.598	10 57 40.67	13.83	0.81	0.71	0.42	-1.55	87.33	6.46	1.13
78	J052610.2+113512	05 26 10.243	11 35 12.31	16.48	1.16	1.22	0.52	-3.35	27.73	6.38	0.40
79	J052615.5+105415	05 26 15.485	10 54 14.67	15.22	0.79	0.73	0.43	1.07	13.64	7.34	0.86
80	J052621.6+113134	05 26 21.603	11 31 33.68	12.73 ^c	1.03 ^c	0.99 ^c	0.25	8.27 ^d	18.93	0.00	0.57 ^e
81	J052633.6+114028	05 26 33.622	11 40 28.22	17.21	1.40	1.49	0.64	6.63	29.10	6.22	0.30
82	J052659.9+104140	05 26 59.911	10 41 40.46	15.14	0.92	0.87	0.57	2.63	26.21	6.73	0.78
83	J052719.1+102547	05 27 19.143	10 25 46.59	17.02	1.20	1.51	0.77	10.30	29.46	6.21	0.29
84	J052737.2+112550	05 27 37.235	11 25 50.21	15.99	1.16	1.33	0.78	3.63	27.17	5.99	0.36
85	J052739.7+112421	05 27 39.697	11 24 21.36	14.92	0.94	0.93	0.55	12.71	26.82	6.38	0.67
86	J052742.4+111518	05 27 42.390	11 15 17.86	16.41	1.04	1.05	0.49	1.48	30.86	6.85	0.55
87	J052742.5+112421	05 27 42.547	11 24 21.36	17.17	1.30	1.42	0.87	9.68	31.76	6.31	0.33
88	J052747.7+111601	05 27 47.730	11 16 01.11	12.63	0.64	0.66	0.43	0.42	24.45	5.93	1.37
89	J052801.9+112624	05 28 01.890	11 26 24.05	17.41	1.22	1.44	0.43	9.32	30.79	6.46	0.32
90	J052818.0+115651	05 28 17.972	11 56 50.67	15.38	1.15	1.18	0.54	36.74	30.05	5.94	0.42
91	J052826.3+110045	05 28 26.346	11 00 44.94	16.57	1.09	1.23	0.59	3.47	25.89	6.47	0.39
92	J052843.7+120446	05 28 43.744	12 04 45.65	17.66	1.53	1.82	0.55	9.59	26.59	5.86	0.19
93	J052846.0+110424	05 28 46.048	11 04 23.57	17.06	1.16	1.39	0.74	9.93	19.04	6.39	0.34
94	J052858.5+104538	05 28 58.521	10 45 37.72	13.14	0.65	0.63	0.27	0.31	65.37 ^f	6.37	1.40
95	J052858.9+105245	05 28 58.943	10 52 45.10	16.31	1.03	1.14	0.58	4.78	27.01	6.55	0.46
96	J052918.1+115158	05 29 18.092	11 51 57.81	14.51	1.03	1.06	0.60	2.33	22.76	5.74	0.52
97	J052918.6+115339	05 29 18.564	11 53 39.12	13.19	0.74	0.75	0.50	0.43	26.05	6.03	1.09
98	J052920.3+124100	05 29 20.254	12 41 00.11	16.47	1.24	1.12	0.52	0.08	22.95	6.59	0.48
99	J052926.7+115145	05 29 26.686	11 51 44.91	15.94	1.12	1.38	0.61	22.88	28.90	5.90	0.34

Table 2—Continued

ID	ID	USNO-A2.0	Coordinates	V	V-R	R-I	$W_{\lambda}(\text{Li})^a$	$W_{\lambda}(\text{H}\alpha)^a$	V_r	log Age ^b	Mass ^b
I Ori	I Ori	R.A.	Decl				\AA	\AA	km s^{-1}	yr	M_{\odot}
100	J052934.2+125622	05 29 34.212	12 56 21.69	14.90	1.12	1.02	0.51	95.43	28.68	5.99	0.55
101	J052946.4+103602	05 29 46.413	10 36 02.00	17.67	1.26	1.48	0.56	5.32	32.25	6.50	0.30
102	J052948.8+110649	05 29 48.819	11 06 48.72	15.95	0.99	0.95	0.51	4.42	27.36	6.85	0.66
103	J052949.4+110105	05 29 49.418	11 01 05.33	16.36	1.06	1.15	0.60	4.58	23.33	6.55	0.45
104	J052951.6+114032	05 29 51.632	11 40 32.01	14.78	0.94	0.96	0.51	4.02	24.66	6.21	0.61
105	J052952.1+120838	05 29 52.065	12 08 38.33	13.29	0.59	0.54	0.30	-0.71	23.59	7.02	1.25
106	J052952.8+120947	05 29 52.770	12 09 47.20	16.12	1.19	1.39	0.58	31.14	26.54	5.93	0.33
107	J052957.7+121207	05 29 57.661	12 12 07.03	15.00	1.00	0.98	0.59	2.75	26.03	6.24	0.59
108	J052958.8+104050	05 29 58.773	10 40 49.64	17.04	1.12	1.33	0.61	3.99	31.49	6.52	0.36
109	J053000.6+121345	05 30 00.632	12 13 44.59	17.92	1.42	1.53	0.40	114.32	23.23	6.46	0.29
110	J053001.9+121310	05 30 01.907	12 13 09.88	12.74	0.71	0.63	0.51	-0.39	31.22	6.01	1.48
111	J053002.0+121336	05 30 02.040	12 13 35.68	13.13	0.70	0.64	0.41	33.76	22.06	6.30	1.38
112	J053003.3+110330	05 30 03.286	11 03 30.41	15.31	1.00	1.08	0.57	4.18	26.51	6.19	0.51
113	J053003.8+120122	05 30 03.816	12 01 21.86	15.24	1.01	0.97	0.58	23.43	24.20	6.39	0.62
114	J053005.7+120937	05 30 05.658	12 09 37.28	16.86	1.32	1.60	0.60	39.03	27.54	5.89	0.26
115	J053013.1+120846	05 30 13.133	12 08 45.96	13.84	0.78	0.77	0.43	22.12	25.33	6.34	1.01
116	J053013.5+130512	05 30 13.452	13 05 12.10	16.12	1.16	1.14	0.56	0.38	30.28	6.38	0.46
117	J053015.2+130010	05 30 15.240	13 00 09.82	17.13	1.14	1.01	0.34	-9.75	14.45	7.40	0.58
118	J053017.1+121541	05 30 17.060	12 15 41.22	16.00	1.03	1.07	0.54	6.09	25.58	6.57	0.52
119	J053025.2+112118	05 30 25.192	11 21 18.02	16.57	1.03	1.21	0.50	1.94	26.83	6.54	0.40
120	J053029.1+123357	05 30 29.091	12 33 56.87	16.83	1.01	1.07	0.24	171.14	24.05	7.02	0.53
121	J053036.1+120641	05 30 36.072	12 06 40.76	17.18	1.18	1.29	0.65	244.76	25.27	6.64	0.37
122	J053036.1+103055	05 30 36.132	10 30 54.58	13.34	0.61	0.54	0.44	6.08	22.33	7.02	1.24
123	J053036.2+123653	05 30 36.213	12 36 53.22	15.17	0.97	0.96	0.28	127.58	26.06	6.42	0.64
124	J053039.6+110232	05 30 39.552	11 02 32.20	16.73	1.09	1.32	0.59	4.45	26.67	6.38	0.36
125	J053051.7+120837	05 30 51.691	12 08 36.63	14.61	0.88	0.82	0.58	42.62	31.71	6.62	0.87
126	J053054.0+124332	05 30 53.966	12 43 31.72	16.85	1.08	1.06	0.22	-2.63	24.49	7.02	0.55
127	J053056.9+115646	05 30 56.896	11 56 46.49	15.09	1.05	1.12	0.72	7.12	17.36	5.94	0.47

Table 2—Continued

ID	ID	USNO-A2.0	Coordinates	V	V-R	R-I	$W_{\lambda}(\text{Li})^a$	$W_{\lambda}(\text{H}\alpha)^a$	V_r	log Age ^b	Mass ^b
I Ori	I Ori	R.A.	Decl				Å	Å	km s ⁻¹	yr	M_{\odot}
128	J053057.0+103253	05 30 56.963	10 32 53.48	15.57	1.02	1.11	0.54	3.27	28.53	6.23	0.48
129	J053057.9+114721	05 30 57.858	11 47 21.37	13.41	0.68	0.69	0.46	0.22	23.10	6.36	1.22
130	J053100.5+113137	05 31 00.482	11 31 37.49	15.64	1.04	1.11	0.56	3.12	29.11	6.26	0.49
131	J053101.0+120414	05 31 01.001	12 04 14.46	16.53	1.16	1.29	0.66	3.55	24.23	6.29	0.37
132	J053101.4+103332	05 31 01.422	10 33 32.07	13.87	0.71	0.75	0.45	0.29	27.82	6.46	1.05
133	J053103.3+102844	05 31 03.252	10 28 43.57	16.31	1.14	1.34	0.74	15.19	29.34	6.20	0.35
134	J053107.9+112527	05 31 07.892	11 25 27.29	16.03	1.15	1.33	0.53	2.36	30.45	6.00	0.35
135	J053108.0+120607	05 31 08.033	12 06 06.51	15.88	1.09	1.20	0.64	4.76	24.77	6.23	0.40
136	J053115.5+121124	05 31 15.511	12 11 23.74	16.36	1.22	1.28	0.50	15.05	23.66	6.25	0.37
137	J053116.0+105151	05 31 15.972	10 51 50.98	17.37	1.23	1.45	0.61	7.80	27.24	6.41	0.32
138	J053116.1+112531	05 31 16.148	11 25 31.28	15.31	0.94	0.96	0.53	12.18	22.68	6.51	0.63
139	J053117.4+111457	05 31 17.374	11 14 56.79	14.17	0.96	0.99	0.60	2.69	40.72	5.73	0.58
140	J053119.0+103458	05 31 19.006	10 34 58.03	16.81	1.12	1.24	0.50	5.69	25.93	6.56	0.39
141	J053119.1+103439	05 31 19.128	10 34 38.55	15.49	0.90	0.91	0.56	1.89	23.55	6.78	0.71
142	J053121.6+120547	05 31 21.633	12 05 46.71	13.76	0.95	0.97	0.48	-0.41	26.37	5.61	0.60
143	J053123.6+120944	05 31 23.600	12 09 44.02	12.83	0.74	0.68	0.45	4.74	23.79	5.95	1.30
144	J053126.9+112333	05 31 26.850	11 23 32.79	16.93	1.16	1.42	0.64	3.24	29.30	6.28	0.33
145	J053127.2+103358	05 31 27.152	10 33 58.28	16.63	1.17	1.42	0.68	4.48	27.15	6.20	0.32
146	J053134.2+110345	05 31 34.151	11 03 45.13	16.86	1.16	1.38	0.49	4.71	28.57	6.30	0.34
147	J053134.6+114930	05 31 34.578	11 49 29.82	15.03	0.98	1.04	0.56	2.57	24.98	6.15	0.54
148	J053134.6+104949	05 31 34.631	10 49 49.07	16.15	1.12	1.26	0.47	4.84	30.21	6.23	0.38
149	J053137.6+115819	05 31 37.604	11 58 18.51	14.64	0.71	0.70	0.20	-14.20	29.19	7.01	0.99
150	J053138.6+114827	05 31 38.584	11 48 26.57	16.08	1.07	1.13	0.62	0.83	24.90	6.43	0.47
151	J053139.9+115048	05 31 39.912	11 50 48.21	16.37	0.87	1.14	0.27	-1.03	18.43	6.69	0.46
152	J053140.5+121047	05 31 40.467	12 10 46.86	15.10	1.05	1.08	0.51	4.32	16.02	6.04	0.51
153	J053143.4+123022	05 31 43.390	12 30 22.24	13.45	0.67	0.64	0.43	15.04	23.10	6.51	1.30
154	J053145.4+113759	05 31 45.392	11 37 58.62	17.27	1.36	1.69	0.75	5.30	28.42	5.93	0.23
155	J053146.3+111520	05 31 46.328	11 15 20.42	14.99	1.00	1.03	0.36	3.84	-34.10 ^f	6.14	0.55

Table 2—Continued

ID	ID	USNO-A2.0	Coordinates	V	V-R	R-I	$W_{\lambda}(\text{Li})^a$	$W_{\lambda}(\text{H}\alpha)^a$	V_r	log Age ^b	Mass ^b
I Ori	I Ori	R.A.	Decl				Å	Å	km s ⁻¹	yr	M_{\odot}
156	J053147.1+104010	05 31 47.107	10 40 09.99	15.18	0.87	0.87	0.24	1.75	86.60	6.76	0.77
157	J053147.5+111451	05 31 47.527	11 14 51.25	17.20	1.38	1.74	0.65	7.88	21.77	5.84	0.21
158	J053147.8+121808	05 31 47.779	12 18 07.70	13.02	0.73	0.68	0.63	1.05	28.03	6.10	1.31
159	J053148.7+130526	05 31 48.697	13 05 26.47	14.53	0.95	0.87	0.50	3.73	25.72	6.36	0.77
160	J053149.2+123201	05 31 49.164	12 32 00.65	14.55	1.02	1.06	0.57	7.99	23.29	5.77	0.52
							0.41 ^h		-17.85 ^f		
									26.57		
161	J053158.5+122247	05 31 58.467	12 22 47.45	15.93	1.16	1.42	0.61 ^h	16.62	113.78 ^f	5.83	0.32
									23.01		
162	J053159.0+103314	05 31 59.006	10 33 13.99	17.10	1.05	1.58	0.66	3.15	29.30	6.20	0.27
163	J053159.3+111046	05 31 59.264	11 10 46.21	17.62	1.12	1.32	0.37	87.44	30.68	6.86	0.36
164	J053159.9+120807	05 31 59.924	12 08 06.73	16.14	1.09	1.25	0.67	3.17	25.43	6.25	0.38
165	J053206.4+122922	05 32 06.406	12 29 22.25	15.23	1.00	1.06	0.67	3.49	25.11	6.19	0.52
166	J053206.5+122405	05 32 06.491	12 24 04.59	14.79	0.79	0.67	0.43	88.70	23.83	7.10	0.97
167	J053206.5+111502	05 32 06.521	11 15 01.85	13.76	0.75	0.77	0.47	1.00	29.91	6.33	1.02
168	J053207.2+115405	05 32 07.194	11 54 04.54	16.20	1.05	1.20	0.59	8.25	24.86	6.34	0.41
169	J053208.0+120715	05 32 07.956	12 07 14.80	13.63	0.82	0.77	0.60	1.10	24.59	6.22	1.02
170	J053212.8+105609	05 32 12.843	10 56 08.57	14.85	0.78	0.79	0.51	0.92	25.59	6.86	0.90
171	J053213.1+111250	05 32 13.069	11 12 49.73	16.30	1.14	1.26	0.65	4.90	25.00	6.27	0.38
172	J053215.4+120934	05 32 15.439	12 09 34.44	16.38	0.98	1.23	0.63	36.51	25.39	6.42	0.39
173	J053218.1+124356	05 32 18.096	12 43 56.30	15.32	1.08	1.07	0.57	30.27	26.27	6.18	0.51
174	J053225.6+123635	05 32 25.617	12 36 35.31	14.75	0.87	0.82	0.65	36.83	20.95	6.70	0.87
175	J053226.2+115424	05 32 26.212	11 54 24.23	15.94	1.16	1.40	0.77	5.06	27.10	5.85	0.33
176	J053227.3+123754	05 32 27.313	12 37 54.44	13.28	0.60	0.58	0.47	0.44	21.65	6.71	1.38
177	J053229.4+120124	05 32 29.356	12 01 23.87	16.15	1.12	1.39	0.62	4.15	25.48	5.98	0.33
178	J053234.7+111253	05 32 34.705	11 12 52.66	16.47	1.10	1.25	0.65	11.10	28.39	6.35	0.38
179	J053246.9+104354	05 32 46.904	10 43 54.43	17.20	1.18	1.42	0.65	4.01	27.52	6.40	0.33
180	J053246.9+123944	05 32 46.920	12 39 44.26	15.19	1.03	0.99	0.57	3.31	23.89	6.30	0.59

Table 2—Continued

ID	ID	USNO-A2.0	Coordinates	V	V-R	R-I	$W_{\lambda}(\text{Li})^a$	$W_{\lambda}(\text{H}\alpha)^a$	V_r	log Age ^b	Mass ^b
I Ori	I Ori	R.A.	Decl				Å	Å	km s ⁻¹	yr	M_{\odot}
181	J053254.9+125323	05 32 54.932	12 53 23.16	16.83	1.53	1.73	0.55	35.16	24.48	5.66	0.20
182	J053255.3+124105	05 32 55.265	12 41 04.52	15.11	1.12	1.24	0.50	17.55	22.90	5.67	0.39
183	J053259.0+114619	05 32 58.978	11 46 19.46	16.51	1.16	1.10	0.52	2.04	23.58	6.71	0.50
184	J053259.2+105256	05 32 59.168	10 52 56.32	14.92	0.91	0.96	0.56	1.83	23.77	6.30	0.62
185	J053259.5+113915	05 32 59.464	11 39 14.65	15.13	0.90	0.96	0.59	5.06	23.52	6.43	0.64
186	J053303.2+105608	05 33 03.152	10 56 08.24	15.65	1.07	1.22	0.68	5.46	26.08	6.06	0.40
187	J053303.4+114748	05 33 03.395	11 47 48.26	14.18	0.72	0.68	0.29	-0.16	25.50	6.79	1.09
188	J053303.9+115806	05 33 03.942	11 58 05.96	16.59	1.17	1.39	0.72 ^h	8.57	-0.12 ⁱ	6.21	0.33
									51.57		
							0.68 ^h		3.86		
									58.34		
189	J053308.9+115355	05 33 08.877	11 53 55.39	17.27	1.33	1.73	0.58	8.76	26.70	5.89	0.21
190	J053722.9+100705	05 37 22.935	10 07 05.16	17.32	1.14	1.39	0.55	9.43	29.23	6.55	0.34
191	J053725.7+094943	05 37 25.651	09 49 43.40	16.77	1.15	1.49	0.65	9.09	26.99	6.16	0.30
192	J053727.2+095003	05 37 27.248	09 50 02.76	16.67	1.01	1.19	0.62	6.64	27.34	6.66	0.42
193	J053732.8+095130	05 37 32.785	09 51 30.01	16.03	1.09	1.31	0.63	10.31	28.80	6.12	0.36
194	J053733.9+094904	05 37 33.940	09 49 04.32	17.04	1.13	1.36	0.61	7.53	27.84	6.45	0.35
195	J053734.2+101357	05 37 34.238	10 13 56.75	17.45	1.20	1.40	0.66	7.65	25.85	6.57	0.33
196	J053753.7+095512	05 37 53.689	09 55 12.29	16.61	1.08	1.28	0.63	4.28	27.96	6.39	0.38
197	J053759.6+094834	05 37 59.607	09 48 34.09	16.53	1.10	1.28	0.64	5.78	28.13	6.33	0.38
198	J053819.6+092817	05 38 19.638	09 28 16.97	16.81	1.20	1.52	0.67	8.43	26.51	6.05	0.28
199	J053830.6+092806	05 38 30.596	09 28 05.92	15.12	0.88	0.86	0.54	4.41	26.21	6.76	0.78
200	J053834.4+094814	05 38 34.447	09 48 13.93	15.52	0.94	1.05	0.59	4.15	26.54	6.39	0.54
201	J053836.6+101709	05 38 36.647	10 17 08.82	16.88	1.09	1.44	0.58	5.24	31.26	6.27	0.32
202	J053840.2+093758	05 38 40.160	09 37 57.76	15.86	0.98	1.02	0.55	2.87	26.99	6.63	0.57
203	J053843.0+095550	05 38 43.039	09 55 49.96	17.43	1.28	1.58	0.75	5.37	28.05	6.23	0.26
204	J053846.3+093219	05 38 46.324	09 32 18.97	16.98	1.22	1.36	0.55	4.01	28.33	6.37	0.35
205	J053859.5+095726	05 38 59.454	09 57 25.94	17.49	1.26	1.50	0.70	10.51	27.43	6.35	0.30

Table 2—Continued

ID	ID	USNO-A2.0	Coordinates	V	V-R	R-I	$W_{\lambda}(\text{Li})^a$	$W_{\lambda}(\text{H}\alpha)^a$	V_r	log Age ^b	Mass ^b
I Ori	I Ori	R.A.	Decl				\AA	\AA	km s^{-1}	yr	M_{\odot}
206	J053906.9+094114	05 39 06.929	09 41 13.65	17.09	1.21	1.53	0.60	3.96	27.50	6.20	0.28
207	J053910.1+094002	05 39 10.131	09 40 01.52	17.29	1.29	1.60	0.73	6.20	27.64	6.11	0.26
208	J053917.3+094208	05 39 17.302	09 42 07.51	14.58	0.80	0.84	0.48	10.87	25.42	6.59	0.83
209	J053921.0+093123	05 39 21.040	09 31 22.63	16.00	1.08	1.06	0.55	1.14	26.78	6.55	0.53
210	J053938.9+093659	05 39 38.948	09 36 58.69	16.11	1.03	1.18	0.62	4.79	25.57	6.35	0.43
211	J053948.0+095103	05 39 48.011	09 51 02.63	17.89	1.30	1.54	0.62	6.09	29.10	6.49	0.28
212	J054002.1+095531	05 40 02.051	09 55 31.40	12.96	0.56	0.52	0.23	0.03	17.39	7.01	1.30
213	J054032.3+100623	05 40 32.323	10 06 23.00	16.20	1.04	1.18	0.59	9.22	28.98	6.39	0.43
214	J054035.2+095415	05 40 35.195	09 54 15.24	13.96	0.75	0.69	0.47	6.44	25.47	6.59	1.11
215	J054037.1+095443	05 40 37.119	09 54 43.13	16.34	1.07	1.16	0.58	1.83	27.68	6.51	0.45
216	J054122.8+100644	05 41 22.800	10 06 43.59	13.30	0.53	0.48	0.31	-1.68	27.67	7.33	1.09
217	J054128.9+095629	05 41 28.916	09 56 29.31	13.72	0.81	0.79	0.53	3.75	26.96	6.24	0.98
218	J054131.7+101026	05 41 31.672	10 10 26.05	14.82	1.01	1.12	0.65 ^h	5.05	19.42 ^j	5.83	0.47
									63.51		
									29.47		
219	J054144.8+091306	05 41 44.842	09 13 06.14	15.13	1.02	1.05	0.64	1.89	28.39	6.16	0.53
220	J054152.3+094019	05 41 52.323	09 40 18.97	16.83	1.22	1.47	0.71	4.40	29.12	6.19	0.31
221	J054153.6+093345	05 41 53.595	09 33 45.13	16.43	1.17	1.37	0.58	7.51	29.11	6.19	0.34
222	J054232.4+093423	05 42 32.442	09 34 22.58	17.03	1.22	1.56	0.54	19.37	27.46	6.09	0.27
223	J054235.0+092634	05 42 35.010	09 26 33.51	16.07	1.16	1.32	0.62	2.52	27.89	6.01	0.36
224	J054236.7+094130	05 42 36.692	09 41 29.88	14.36	0.91	0.95	0.61	3.72	26.26	5.95	0.62
225	J054255.0+091501	05 42 54.996	09 15 01.47	15.17	1.04	1.13	0.60	7.82	28.75	5.97	0.46
226	J054315.4+092932	05 43 15.411	09 29 32.05	14.95	0.82	0.86	0.21	-0.80	23.36	6.71	0.79
227	J054320.9+090607	05 43 20.920	09 06 07.12	13.05	0.77	0.78	0.31	52.76	-5.22 ^f	5.86	1.01
									58.60		
228	J054323.2+090532	05 43 23.220	09 05 31.88	13.37	0.80	0.79	0.50	0.41	26.04	5.97	0.97
229	J054324.7+090609	05 43 24.742	09 06 08.62	13.29	0.75	0.72	0.51	-0.02	24.64	6.17	1.15
230	J054328.3+093709	05 43 28.339	09 37 08.62	13.01	0.79	0.83	0.28	1.10	24.16	5.64	0.87

Table 2—Continued

ID	ID	USNO-A2.0	Coordinates	V	V-R	R-I	$W_{\lambda}(\text{Li})^a$	$W_{\lambda}(\text{H}\alpha)^a$	V_r	log Age ^b	Mass ^b
IOr	IOr	R.A.	Decl				\AA	\AA	km s^{-1}	yr	M_{\odot}
231	J054332.2+090924	05 43 32.192	09 09 24.33	14.71	0.96	0.99	0.49	49.93	22.24	6.03	0.58
232	J054333.6+091656	05 43 33.580	09 16 56.41	14.96	0.98	1.17	0.60	3.07	26.61	5.83	0.43
233	J054336.6+092456	05 43 36.629	09 24 55.50	15.06	1.00	1.02	0.66	4.83	24.16	6.17	0.55
234	J054342.1+100221	05 43 42.078	10 02 20.83	14.43	0.88	0.90	0.52	4.10	28.29	6.24	0.72
235	J054344.6+095301	05 43 44.610	09 53 01.49	13.85	0.86	0.95	0.58	2.54	30.40	5.72	0.62
236	J054352.3+091700	05 43 52.338	09 17 00.32	17.18	1.28	1.64	0.63	5.27	25.68	6.00	0.24
237	J054355.6+094831	05 43 55.561	09 48 30.96	15.17	1.03	1.11	0.64	2.84	23.27	6.00	0.48
238	J054356.6+091817	05 43 56.581	09 18 16.90	17.30	1.23	1.44	0.62	26.71	27.87	6.39	0.32
239	J054401.6+091721	05 44 01.574	09 17 20.97	15.64	1.00	1.05	0.67	4.64	25.98	6.42	0.54
240	J054407.3+090638	05 44 07.262	09 06 38.06	14.65	0.91	0.83	0.54	86.96	25.67	6.58	0.84
241	J054409.0+090915	05 44 09.002	09 09 15.09	14.10	0.87	0.82	0.45	27.80	25.04	6.31	0.89
242	J054410.6+091246	05 44 10.588	09 12 45.52	14.18	0.73	0.67	0.49	-0.35	27.23	6.81	1.10
243	J054414.9+090808	05 44 14.883	09 08 08.06	17.05	1.19	1.54	0.63	19.47	28.42	6.19	0.28
244	J054417.3+091059	05 44 17.344	09 10 58.87	14.07	0.93	0.93	0.44	96.46	24.79	5.83	0.65
245	J054419.2+091235	05 44 19.208	09 12 34.64	14.79	1.05	1.19	0.66	5.45	26.73	5.57	0.41
246	J054421.9+090853	05 44 21.852	09 08 52.87	15.42	1.19	1.33	0.68	25.88	25.17	5.67	0.35
247	J054422.9+091035	05 44 22.884	09 10 35.06	16.09	1.08	1.19	0.62	13.73	28.63	6.29	0.42
248	J054423.2+091204	05 44 23.209	09 12 03.79	12.04	0.59	0.56	0.41	3.27	26.26	6.15	2.00
249	J054426.0+090701	05 44 25.965	09 07 00.61	14.21	0.84	0.85	0.54	12.08	27.08	6.29	0.79
250	J054427.0+091043	05 44 26.952	09 10 43.08	17.08	1.16	1.33	0.74	22.97	34.76	6.52	0.36
251	J054436.3+095144	05 44 36.278	09 51 44.06	16.81	1.12	1.32	0.60	5.29	30.08	6.41	0.36
252	J054437.0+091320	05 44 36.974	09 13 19.89	16.94	1.29	1.63	0.50	33.09	26.23	5.90	0.25
253	J054437.0+091321	05 44 36.983	09 13 21.05	16.91	1.29	1.61	0.60	37.33	26.43	5.91	0.25
254	J054437.6+100414	05 44 37.602	10 04 14.39	12.53	0.49	0.47	0.24	-1.57	14.95	7.02	1.35
255	J054444.6+092319	05 44 44.644	09 23 18.56	15.21	1.03	1.19	0.60	21.24	31.46	5.90	0.41
256	J054446.6+091121	05 44 46.586	09 11 21.49	16.80	1.14	1.34	0.52	32.16	25.70	6.35	0.35
257	J054447.0+091752	05 44 47.014	09 17 52.03	14.90	0.82	0.82	0.49	1.56	22.73	6.80	0.86
258	J054452.8+091305	05 44 52.816	09 13 05.18	14.60	0.84	0.76	0.41	-0.22	26.13	6.79	0.97

Table 2—Continued

ID	ID	USNO-A2.0	Coordinates	V	V-R	R-I	$W_\lambda(\text{Li})^a$	$W_\lambda(\text{H}\alpha)^a$	V_r	log Age ^b	Mass ^b
IOri	IOri	R.A.	Decl				Å	Å	km s ⁻¹	yr	M_\odot
259	J054504.1+090452	05 45 04.115	09 04 52.37	17.04	1.35	1.38	0.66	4.79	27.09	6.29	0.34
260	J054521.6+090545	05 45 21.556	09 05 45.29	16.68	1.30	1.50	0.75	4.35	27.27	5.98	0.29
261	J054553.3+091303	05 45 53.280	09 13 02.70	14.02	0.87	0.91	0.41	1.13	18.98	5.89	0.69
262	J054557.4+083749	05 45 57.420	08 37 48.67	17.24	1.43	1.66	0.75	15.10	26.05	5.93	0.24
263	J054649.2+085815	05 46 49.157	08 58 14.59	13.43	0.87	0.83	0.48	3.20	27.43	5.83	0.86
264	J055003.9+080708	05 50 03.925	08 07 08.34	12.89	0.55	0.49	0.32	-1.92	26.67	7.03	1.29
265	J055017.0+081525	05 50 16.993	08 15 24.58	14.47	0.97	0.96	0.50	6.03	27.32	5.95	0.61
266	J055104.7+082303	05 51 04.666	08 23 02.95	12.90	0.56	0.56	0.29	-0.68	24.40	6.75	1.48

^aPositive $W_\lambda(\text{Li})$ values indicate *absorption*. Positive $W_\lambda(\text{H}\alpha)$ values indicate *emission*.

^bAges and masses are interpolated from the Palla & Stahler (1999) stellar evolution models.

^cThe photometry presented is from the lower-quality 1998 data.

^dThis star shows a strong P Cygni profile.

^eThis star is outside the age/mass grid.

^fDouble-lined spectrum.

^gThese stars have one $W_\lambda(\text{Li})$ above 0.2Å and one below.

^h W_λ measured from the combined light of both components.

ⁱTwo observations of a blended double-line spectrum. The first pair are JD2451235.67 while the second pair are two days later (JD2451237.68).

^jThe first pair are from a blended double-line spectrum (JD2451564.82). A second spectrum about three weeks later (JD2451586.65) was not resolvable as two spectra.

Table 3. Sample Completeness

Field	Completeness	PMS Stars	DIL Stars
1	20.9%	3	0
2	95.0%	30	7
3	28.9%	3	0
4	90.3%	15	0
5	97.8%	26	1
6	92.5%	72	2
7	88.8%	30	0
8	92.1%	11	0
9	93.2%	45	9
10	85.3%	12	3
11	86.1%	19	9

Table 4. Massive Star Photometry

HD	PPM	SpT ^a	V	m.e.	b-y	m.e.	m_1	m.e.	c_1	m.e.	N_{vby}	β	m.e.	N_β	Ref
34989	148818	B2	5.788	0.000	-0.022	0.004	0.065	0.008	0.006	0.007	2	2.616	0.003	1	(1)
35729	120965	B3	8.965	0.008	0.186	0.009	0.198	0.007	0.727	0.005	2	2.768	0.006	1	(1)
36104	121014	B8	7.040	0.011	-0.052	0.004	0.140	0.008	0.451	0.003	3	2.719	0.003	3	(2)
36262	121039	B3	7.608	0.005	-0.055	0.004	0.114	0.006	0.271	0.004	2	2.685	0.005	1	(1)
36267	149063	B3	4.207	0.000	-0.062	0.001	0.094	0.003	0.438	0.002	2	2.722	0.001	1	(1)
36653	121110	B3	5.611	0.001	-0.060	0.002	0.111	0.004	0.322	0.006	2	2.676	0.002	1	(1)
36822	149155	B0	4.405	0.005	-0.027	0.001	0.026	0.003	-0.042	0.000	2	2.591	0.001	1	(1)
36824	149151	B5	6.721	0.003	-0.074	0.000	0.113	0.000	0.233	0.004	2	2.672	0.004	1	(1)
36861	149166	O8	3.409	0.001	-0.029	0.003	-0.003	0.007	-0.084	0.003	2	2.580	0.001	1	(1)
36881	121138	B8	5.600	0.005	0.135	0.002	0.053	0.005	0.982	0.007	2	2.716	0.003	1	(1)
36894	149173	B9	7.606	0.001	-0.051	0.005	0.123	0.008	0.214	0.006	2	2.668	0.011	2	(2)
36895	149168	B3	6.722	0.004	-0.047	0.004	0.105	0.007	0.167	0.004	3	2.664	0.005	6	(2)
37035	149193	B9	8.662	0.005	-0.021	0.004	0.128	0.009	0.471	0.007	3	2.731	0.008	5	(2)
37051	149199	B9	9.068	0.017	0.004	0.004	0.139	0.007	0.827	0.003	2	2.810	0.007	2	(2)
37232	149227	B3	6.113	0.006	-0.073	0.001	0.097	0.002	0.082	0.007	2	2.636	0.003	1	(1)
38672	121410	B5	6.689	0.003	-0.046	0.003	0.128	0.007	0.614	0.003	2	2.735	0.004	1	(1)
245140	149162	B9	9.200	0.004	0.043	0.000	0.129	0.002	0.650	0.003	2	2.767	0.009	2	(2)
245168	149165	B9	9.676	0.002	0.041	0.001	0.163	0.005	0.909	0.006	3	2.873	0.014	4	(2)
245185	...	A5 ^b	9.92	0.06	0.04	0.01	0.16	0.02	0.91	0.02	3	2.82	0.01	3	(3)
245203	149169	B8	7.473	0.008	-0.021	0.002	0.098	0.010	0.284	0.018	2	2.670	0.006	2	(2)

^aSpectral types are reported from the PPM catalog, except for HD 245185 which is from the HD catalog.

^bTerranegra et al. (1994) find a photometric spectral type of B9.5III-V for this Herbig Ae-Be star.

References. — (1) Helt & Olsen; (2) Kaltcheva & Olsen; (3) Terranegra et al. (1994).

Table 5. Massive Star Derived Data

HD	E_{B-V}	$\log T_{\text{eff}}$	$\log L/L_{\odot}$	M/M_{\odot}	D (pc)	Error ^a
34989	0.12	4.42	4.17	11.9	226	19%
35729	0.32	4.09	2.37	3.6		
36104	0.02	4.17	2.97	5.0	364	32%
36262	0.04	4.26	2.97	5.7	246	23%
36267	0.01	4.18	4.10	6.3	88	9%
36653	0.03	4.23	3.68	7.7	157	16%
36822	0.12	4.45	4.79	17.9	302	23%
36824	0.02	4.28	3.34	6.7	893	82%
36861	0.12	4.48	5.24	26.8	324	25%
36881	0.21	4.02	3.45	4.7	448	37%
36894	0.06	4.29	3.06	6.2		
36895	0.07	4.32	3.50	7.6	426	35%
37035	0.06	4.17	2.35	3.9	403	48%
37051	0.05	4.04	1.90	2.8		
37232	0.04	4.36	3.81	9.3	266	24%
38672	0.01	4.11	2.96	4.6	297	31%
245140	0.13	4.10	2.07	3.3		
245168	0.09	4.00	1.64	2.5		
245185	0.09	4.02	1.57	2.4		
245203	0.09	4.25	3.07	5.9		

^aThe distance is the inverse of the Hipparcos parallax. The error is the parallax fractional error.

Table 6. Error Analysis

Category	HD 36861				HD 36822			
	Age		Mass		Age		Mass	
	-1σ	$+1\sigma$	-1σ	$+1\sigma$	-1σ	$+1\sigma$	-1σ	$+1\sigma$
Normal	5.5 Myr		23.9 M_{\odot}		7.5 Myr		16.9 M_{\odot}	
V	0.0%	0.0%	0.0%	0.0%	0.0%	0.0%	-0.1%	0.1%
$b - y$	-0.3%	0.3%	-0.4%	0.4%	-0.2%	0.1%	-0.1%	0.2%
c_1	-0.8%	0.9%	-0.5%	0.5%	0.0%	0.0%	0.0%	0.0%
Distance	-12.6%	5.6%	-7.1%	12.3%	-1.9%	3.5%	-6.7%	5.8%
Binarity	12.5%		-19.7%		-8.8%		-15.9%	

Table 7. Follow-up Data for DIL Stars

DIL ID	USNO A2.0 ID	Coordinates (2000.0)		Our ID
1	0900-01498595	05:16:56.261	07:16:12.44	
2	0975-01581572	05:25:09.988	13:39:21.48	
3	0975-01597108	05:26:09.527	11:23:36.03	
4	0975-01597479	05:26:10.896	08:34:05.17	
5	0975-01600198	05:26:21.603	11:31:33.68	80
6	0975-01619140	05:27:38.304	11:25:39.39	
7	0975-01620328	05:27:43.114	14:46:14.01	
8	0975-01619486	05:27:39.697	11:24:21.36	85
9	0975-01628975	05:28:17.972	11:56:50.67	90
10	0975-01636413	05:28:48.504	11:20:57.96	
11	0975-01641178	05:29:08.382	11:52:12.87	
12	0975-01644925	05:29:23.934	11:51:57.72	
13	0975-01647321	05:29:34.212	12:56:21.69	100
14	0975-01653632	05:30:00.632	12:13:44.59	109
15	0975-01653941	05:30:01.907	12:13:09.88	110
16	0975-01653973	05:30:02.040	12:13:35.68	111
17	0975-01654400	05:30:03.816	12:01:21.86	113
18	0975-01654638	05:30:04.786	12:13:09.28	
19	0975-01656626	05:30:13.133	12:08:45.96	115
20	0975-01660632	05:30:29.091	12:33:56.87	120
21	0975-01662407	05:30:36.213	12:36:53.22	123
22	0975-01662364	05:30:36.072	12:06:40.76	121
23	0975-01664091	05:30:42.972	11:38:17.76	
24	0975-01666218	05:30:51.691	12:08:36.63	125
25	0975-01667146	05:30:55.331	08:40:52.70	
26	0975-01674412	05:31:23.600	12:09:44.02	143
27	0975-01674730 ^a	05:31:24.702	12:12:08.72	
28	0975-01675287	05:31:26.749	11:01:22.27	
29	0975-01675622	05:31:28.018	12:09:10.85	
30	0975-01679906	05:31:43.390	12:30:22.24	153
31	0975-01680777	05:31:46.639	12:57:27.85	
32	0975-01681485	05:31:49.164	12:32:00.65	160
33	0975-01684147	05:31:58.467	12:22:47.45	161
34	0975-01686413	05:32:06.491	12:24:04.59	166
35	0975-01689129	05:32:15.439	12:09:34.44	172
36	0975-01689909	05:32:18.096	12:43:56.30	173
37	0975-01689808	05:32:17.704	12:23:58.86	
38	0975-01690206	05:32:19.083	12:24:22.76	

Table 7—Continued

DIL ID	USNO A2.0 ID	Coordinates (2000.0)		Our ID
39	0975-01691081	05:32:21.996	12:18:04.71	
40	0975-01690466	05:32:19.868	09:44:24.42	
41	0975-01692173	05:32:25.617	12:36:35.31	174
42	0975-01692835 ^b	05:32:27.815	12:53:14.15	
43	0975-01692199	05:32:25.715	10:29:45.05	
44	0975-01694143	05:32:32.063	10:44:18.12	
45	0975-01694144	05:32:32.064	09:32:50.44	
46	0975-01695540	05:32:36.395	12:26:19.18	
47	0975-01697597	05:32:43.046	12:21:08.42	
48	0975-01700083	05:32:51.276	11:59:48.57	
49	0975-01703275 ^c	05:33:02.085	11:37:11.62	
50	0975-01704678 ^c	05:33:06.700	11:46:47.98	
51	0975-01722293	05:34:04.135	12:24:23.20	
52	0975-01722552	05:34:04.966	09:57:04.01	6
53	0975-01739062	05:34:57.360	10:57:35.71	
54	0975-01748251	05:35:25.378	10:08:38.42	36
55	0975-01752685	05:35:38.932	10:32:28.01	
56	0975-01754813	05:35:45.559	10:36:54.00	
57	0975-01766266	05:36:19.582	12:46:19.11	
58	0975-01775145	05:36:45.641	09:04:19.88	
59	0975-01828002	05:39:12.691	09:15:52.63	
60	0975-01828907	05:39:15.178	09:50:04.39	
61	0975-01829634	05:39:17.302	09:42:07.51	208
62	0975-01838431	05:39:41.822	09:09:29.16	
63	0975-01840345	05:39:46.973	10:59:15.00	
64	0975-01844912	05:39:59.431	09:44:23.84	
65	0975-01845737	05:40:01.592	08:08:15.31	
66	0975-01861497	05:40:45.008	12:21:23.08	
67	0975-01860761	05:40:43.094	09:25:35.04	
68	0975-01864840	05:40:54.413	08:54:18.90	
69	0975-01875096	05:41:22.590	09:01:44.96	
70	0975-01877635 ^d	05:41:29.570	09:07:20.16	
71	0975-01879639	05:41:35.014	11:39:23.70	
72	0975-01879867	05:41:35.632	09:07:51.30	
73	0975-01893809	05:42:13.758	08:43:56.83	
74	0975-01902866	05:42:37.770	08:51:02.89	
75	0975-01910928	05:42:59.320	09:09:52.59	
76	0975-01915637	05:43:11.658	09:36:15.01	

Table 7—Continued

DIL ID	USNO A2.0 ID	Coordinates (2000.0)		Our ID
77	0975-01919100	05:43:20.920	09:06:07.12	227
78	0975-01923451	05:43:32.192	09:09:24.33	231
79	0975-01931979	05:43:53.362	09:07:19.00	
80	0975-01933469 ^e	05:43:57.031	09:16:31.17	
81	0975-01937551	05:44:07.262	09:06:38.06	240
82	0975-01938239	05:44:09.002	09:09:15.09	241
83	0975-01941558	05:44:17.344	09:10:58.87	244
84	0975-01938141	05:44:08.761	09:19:10.15	
85	0975-01943327	05:44:21.852	09:08:52.87	246
86	0975-01951155	05:44:41.358	08:56:59.37	
87	0975-01952462	05:44:44.644	09:23:18.56	255
88	0975-01978798	05:45:50.994	10:02:27.99	
89	0975-01999207	05:46:42.944	08:43:52.15	
90	0975-02024029	05:47:45.456	08:33:21.01	
91	0975-02026277	05:47:51.120	11:15:14.23	
92	0975-02025350	05:47:48.844	08:33:26.09	
93	0975-02032661	05:48:06.493	09:53:43.49	
94	0975-02033474	05:48:08.534	09:54:01.22	
95	0975-02039974	05:48:24.194	08:22:52.75	
96	0900-01984369	05:48:44.176	04:36:04.87	
97	0975-02086044	05:50:12.846	08:14:31.81	
98	0900-02011995	05:50:37.002	04:47:46.95	
99	0975-02160135	05:53:01.211	09:59:51.95	

^aDIL 27 appears to be part of a very close pair. We have indicated the likely match, but the other is at 05:31:24.660 12:12:09.71.

^bDIL 42 is not marked on the DIL finding charts. We found the star in Haro, Iriarte & Chavira (1953), but there are too few stars visible in their finding chart to be absolutely sure this is the right one.

^cDIL 49 and 50 have reversed names in the DIL catalog. DIL 49 should be “H 6-70” while DIL 50 should be “H 6-69”. Column 8 of the DIL catalog should be reversed for these stars as well.

^dDIL 70 is unclearly marked on both the DIL and Manova finding charts. We have indicated the likely match, but another possibility is at 05:41:29.597 09:07:11.21.

^eDIL 80 is unclearly marked on both the DIL and Manova finding charts. We have indicated the likely match, but another possibility is at 05:43:57.008 09:16:25.65.

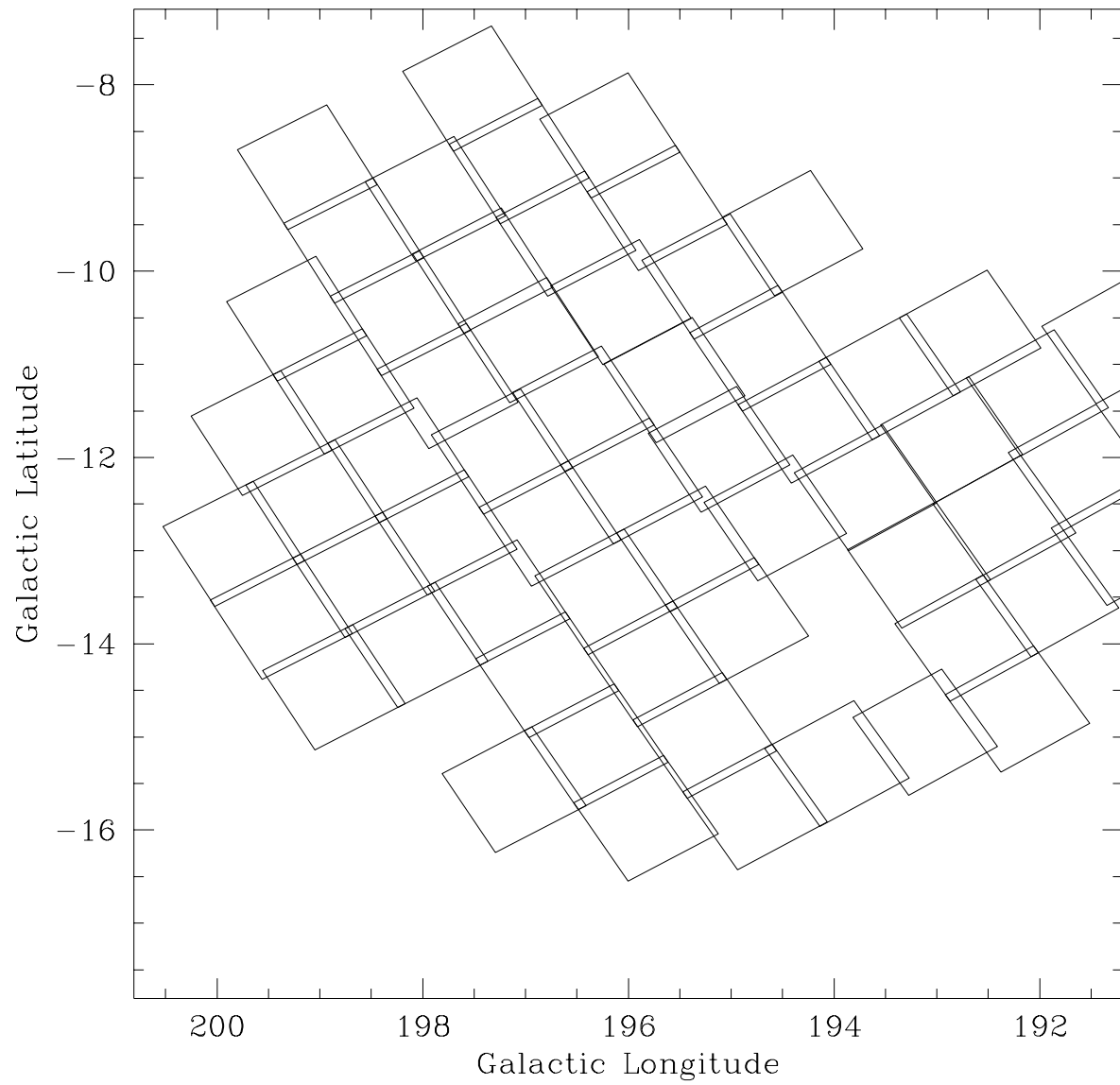


Fig. 1.— CCD fields observed in 1999.

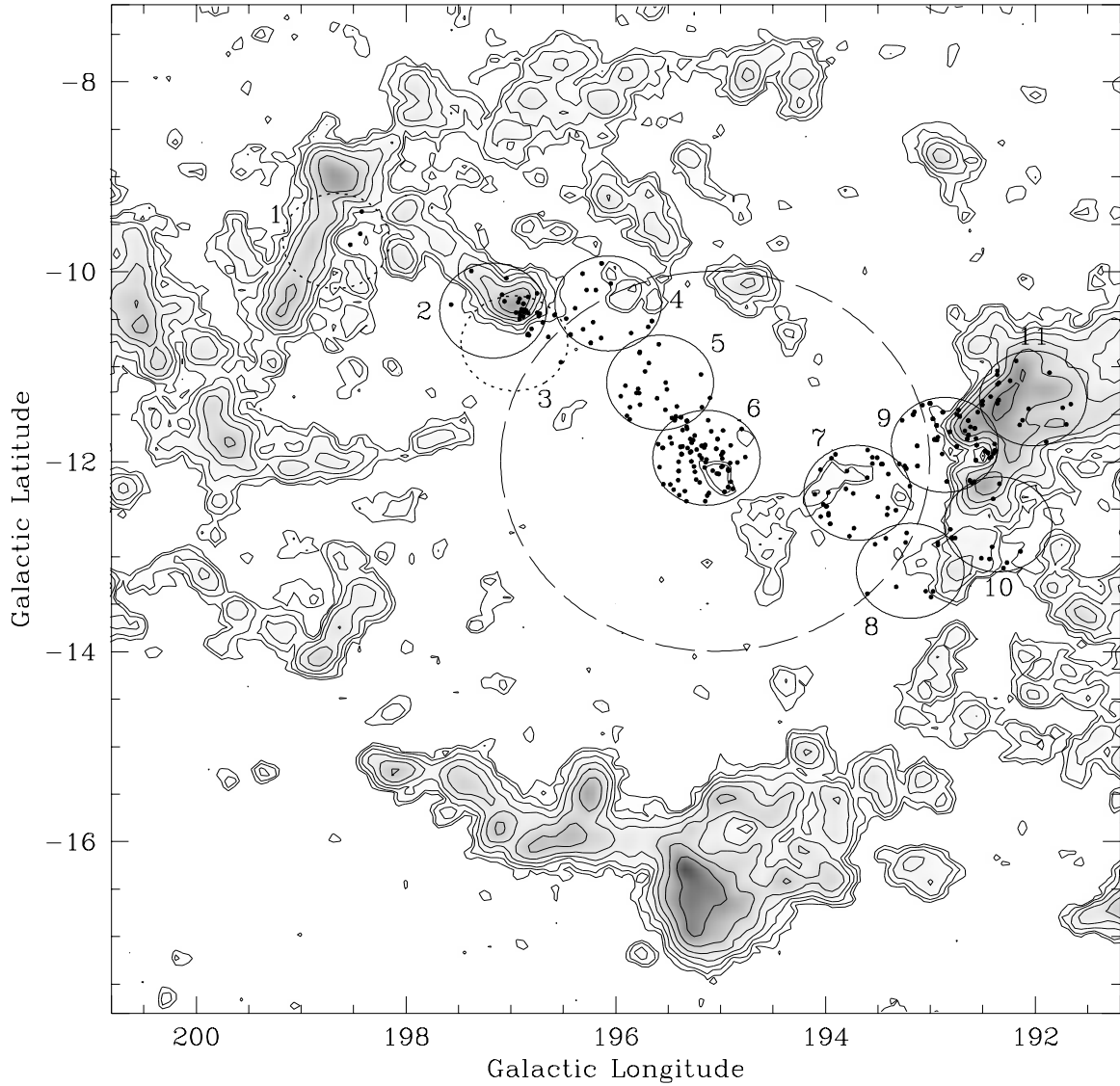


Fig. 2.— Map of our survey region overlaid on the CO map of Lang & Mashedier (1998). The circles mark our WIYN MOS target fields (labeled with numbers), with dashed lines indicating incompletely surveyed fields. The dots mark the position of stars with “strong” lithium absorption. Paper I focused on what we now call Field 6.

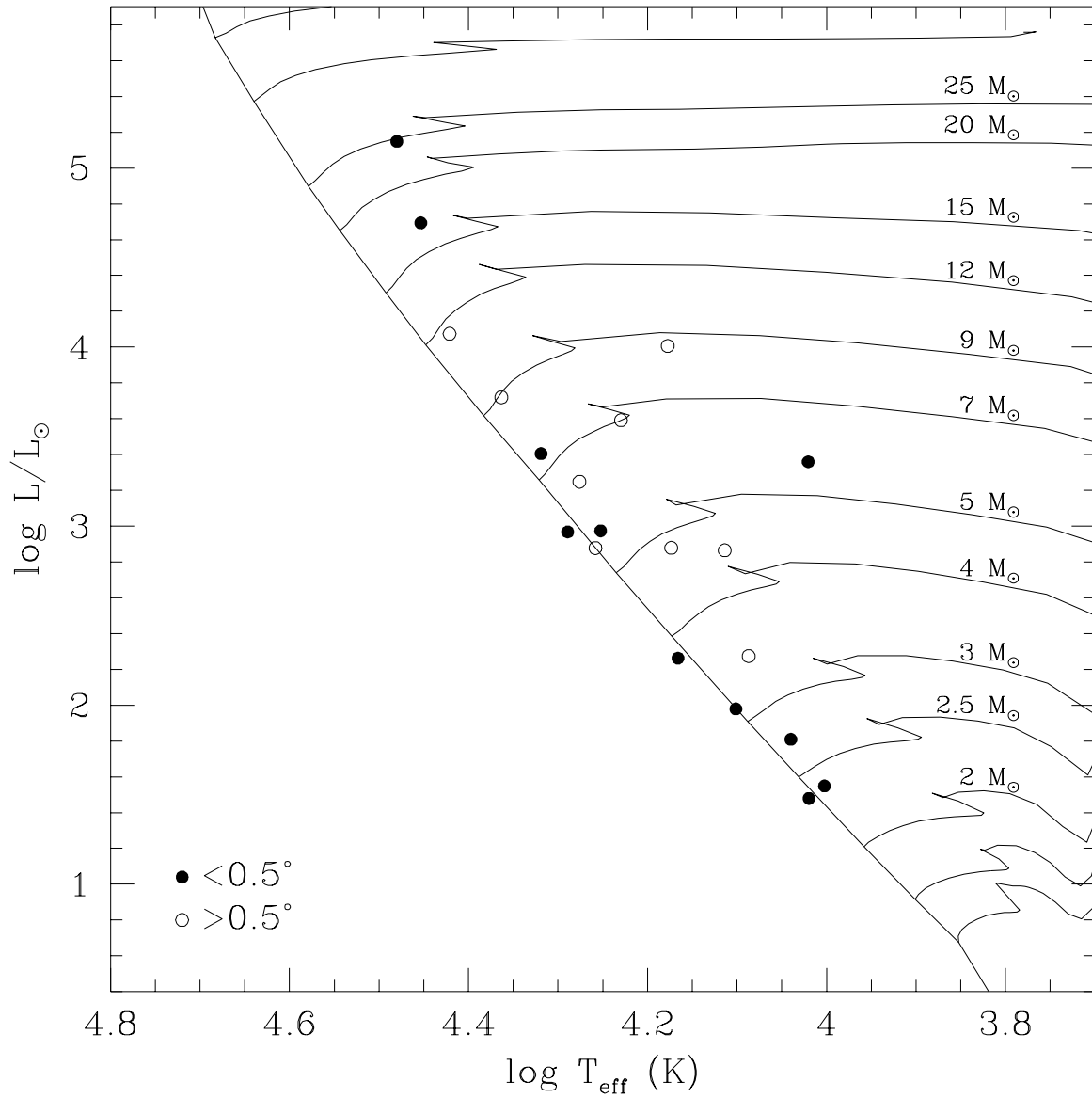


Fig. 3.— HR diagram of OB stars (assuming a distance of 450 pc) with Schaller et al. (1992) evolutionary tracks. The symbols indicate stars within 0.5° of λ Ori (solid) or more than 0.5° away (open).

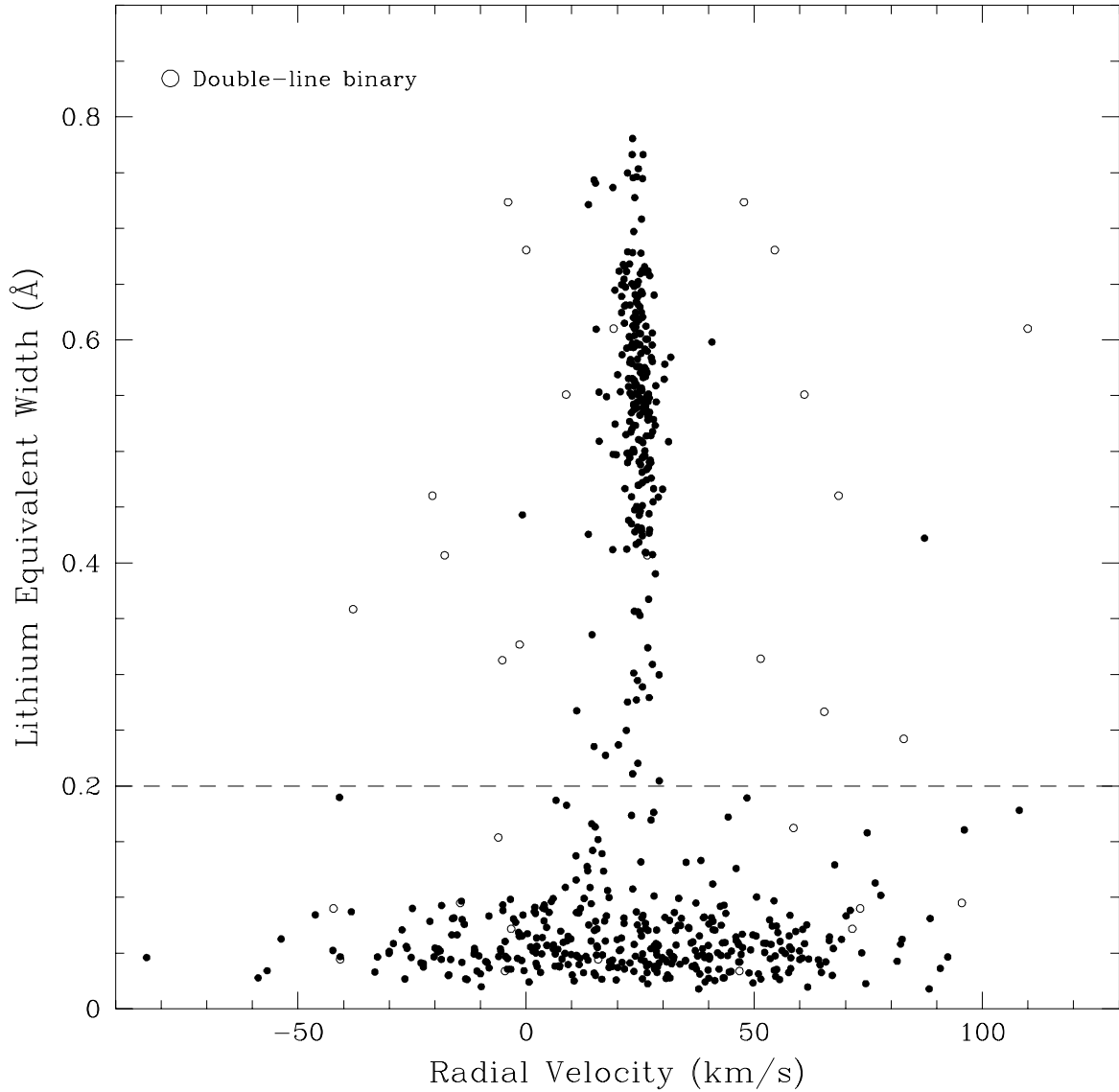


Fig. 4.— Discrimination between field stars and low-mass members of the λ Ori association. Displayed are the 648 stars for which we have detected lithium $\lambda 6708$ absorption. Those 266 stars with lithium equivalent widths greater than 0.2\AA are taken to be PMS association members. Excluding spectroscopic binaries, these strong-lithium stars have a mean radial velocity of 24.5 km/s and a velocity dispersion of only 2.3 km/s , confirming membership in the association.

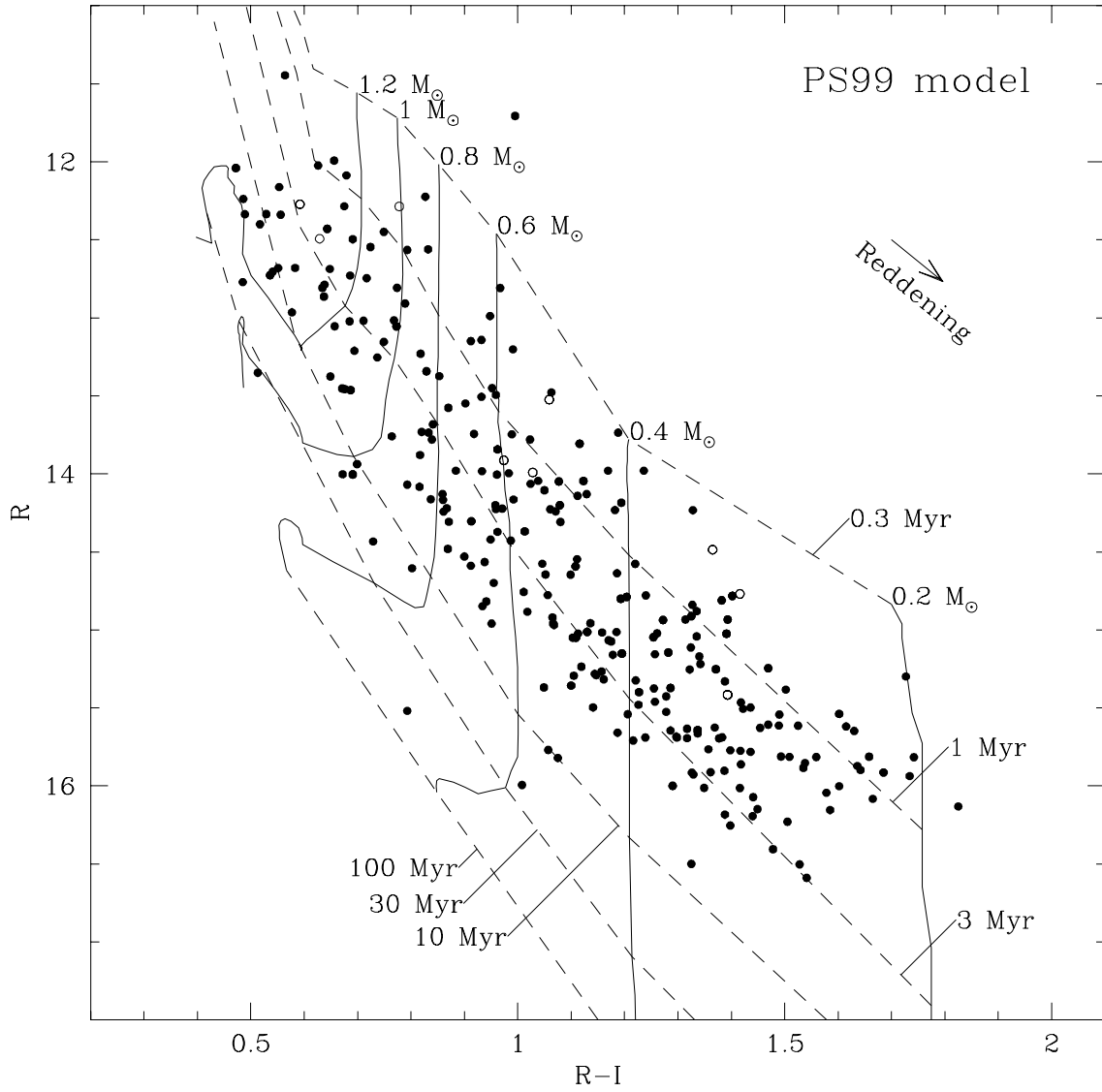


Fig. 5.— Comparison of strong-lithium stars to the PS99 evolutionary tracks and isochrones. The tracks are converted into the observed plane by the procedure described in the text. Double-line binaries are marked as open circles.

BCAH98

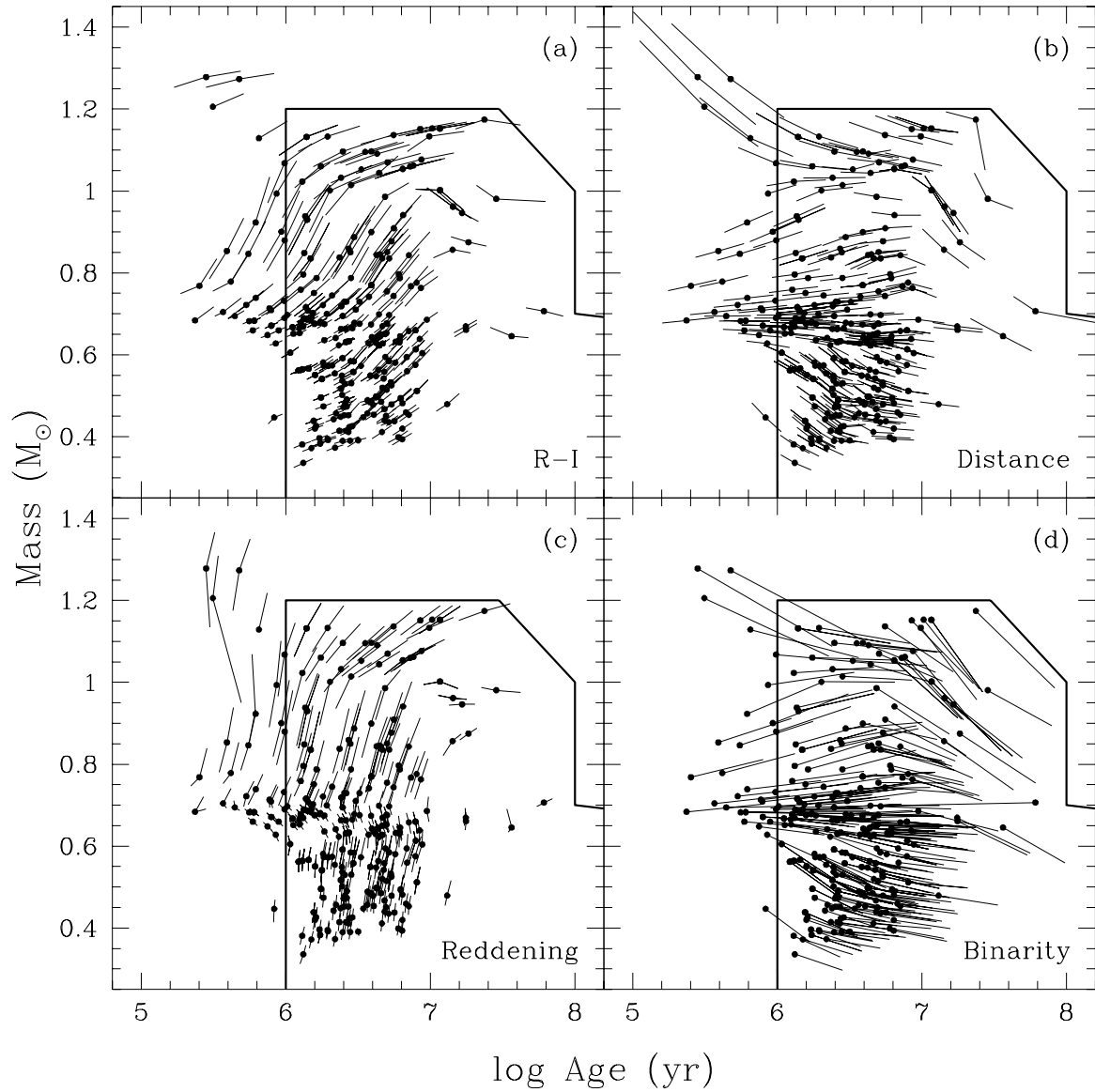


Fig. 6.— Visualization of the errors contributed by various parameters. Typical errors in $R-I$, distance and reddening as well as luminosity change due to an equal-mass binary are propagated into age and mass space, via the BCAH98 model. The outline marks the limits of the BCAH98 model grid. Stars outside this box have extrapolated ages and masses.

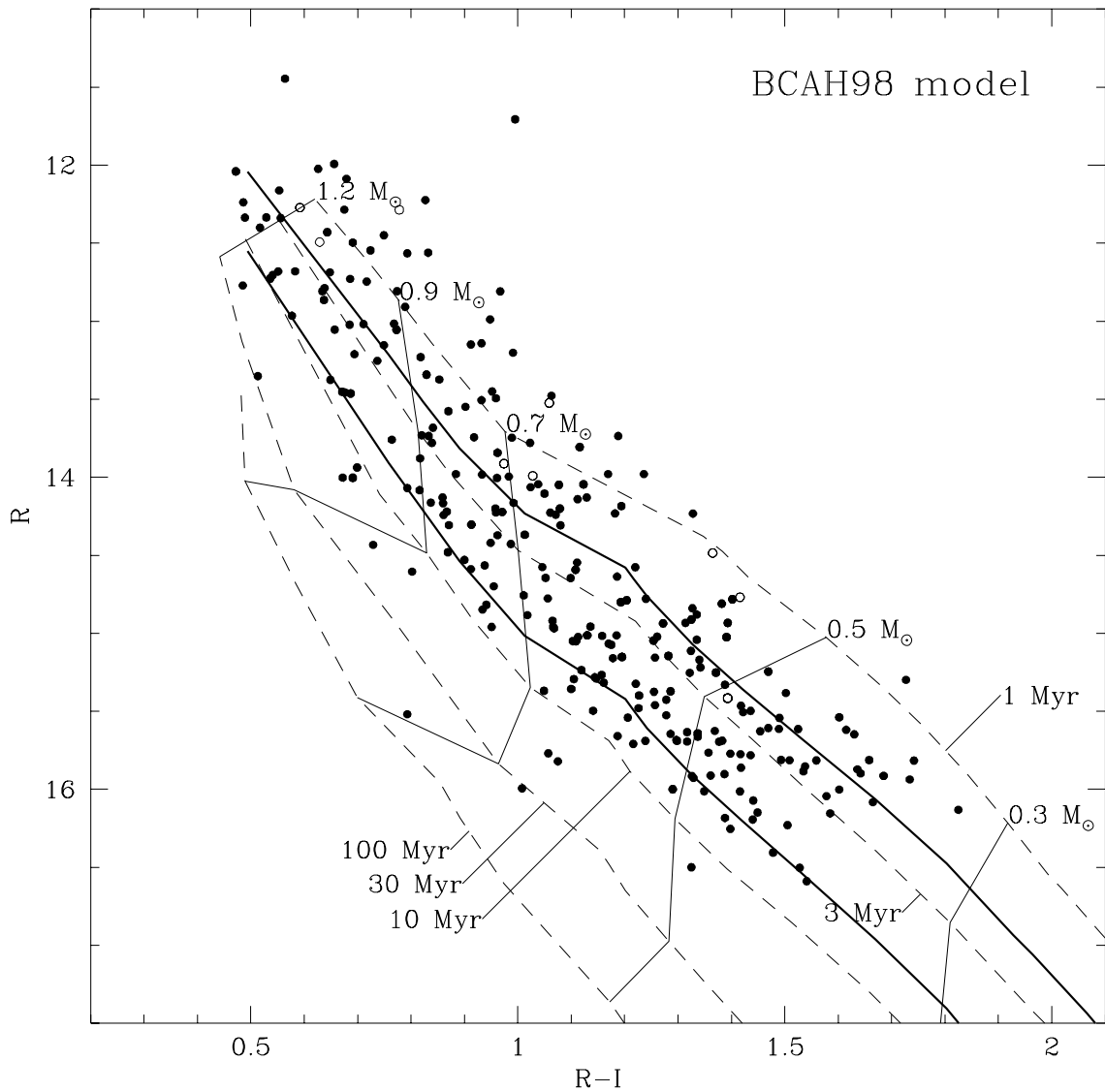


Fig. 7.— Comparison of the predicted age spread for a 5 Myr coeval population model versus the observed population. The model is based on the BCAH98 isochrones. The predicted age spread (heavy lines) is computed from the measured photometric error, an assumed 10% distance error and a 100% binary population with a Miller & Scalo (1979) secondary mass distribution. 53% of the stars fall within the dark lines, where the coeval model predicts 90%, indicating a real age spread in the PMS stellar population.

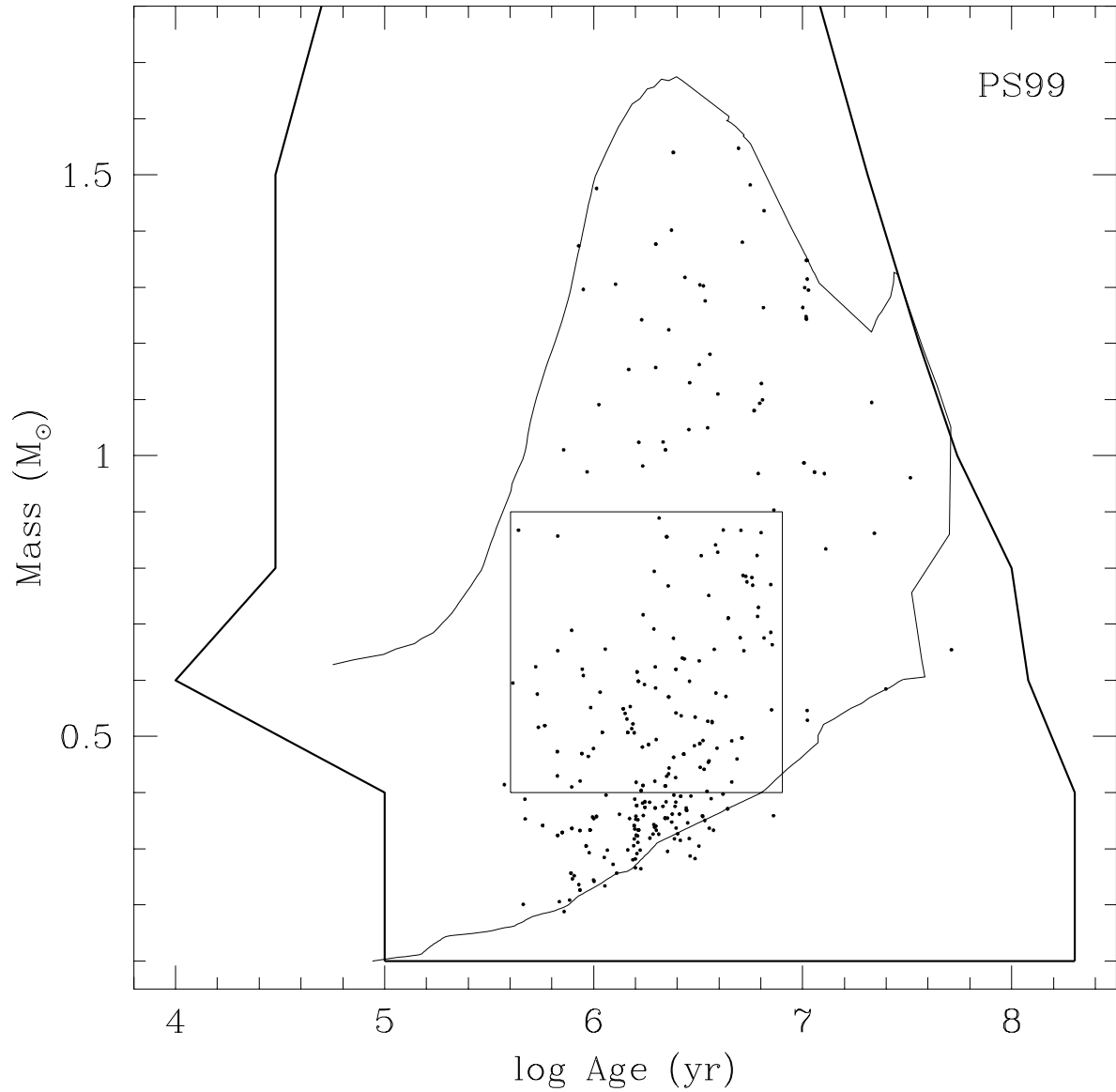


Fig. 8.— The age and mass limits of our PMS star survey. The heavy line marks the limits of the PS99 model grid. The curved line is our photometric boundaries transformed into the age-mass plane via the PS99 grid. The rectangle marks a bias-free region defined by $0.4 < \text{age} < 8$ Myr and $0.4 < M < 0.9M_{\odot}$. The dots are our newly detected PMS stars.

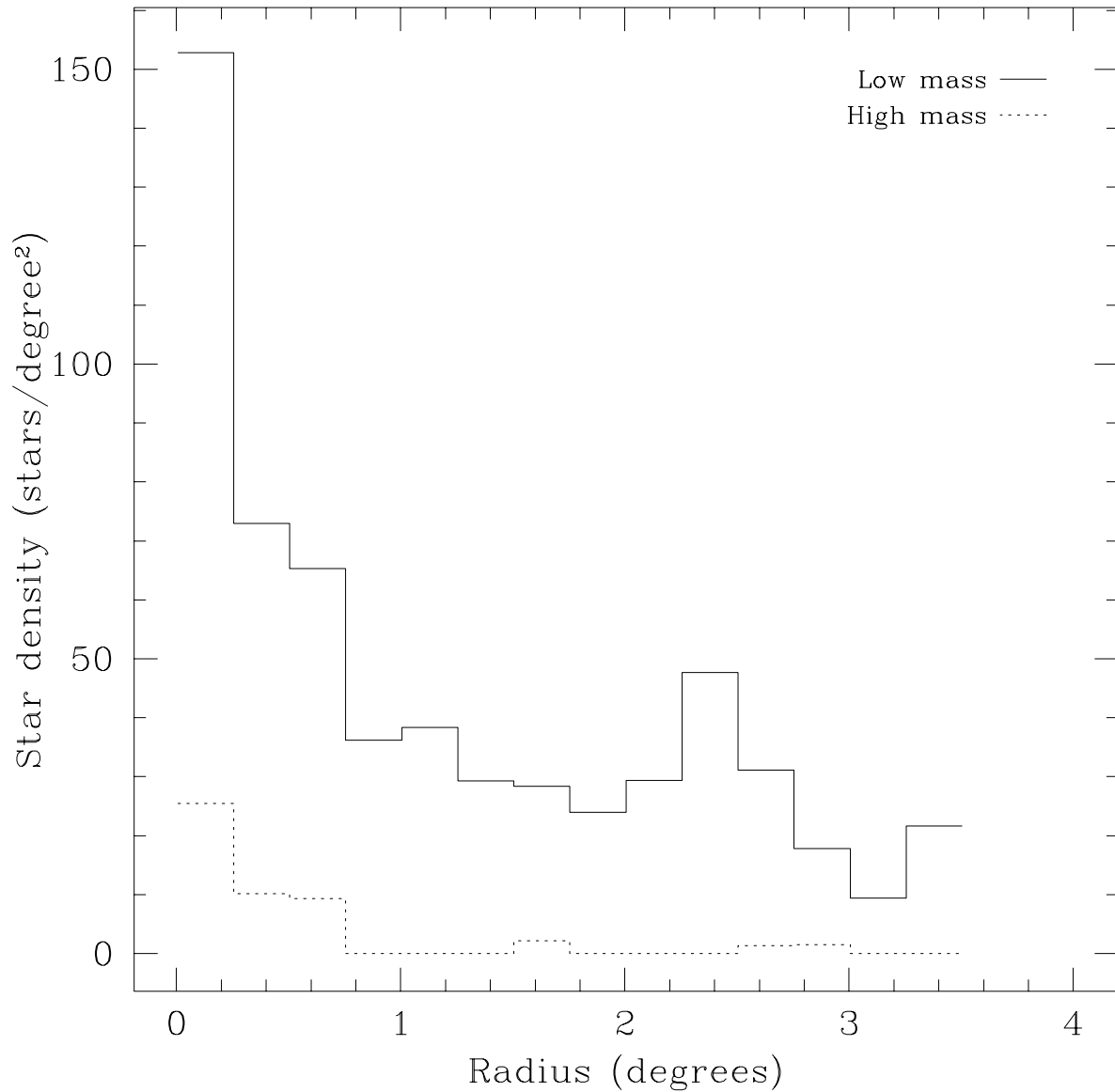


Fig. 9.— Stellar surface density of low-mass association members as a function of radius. Also shown is the distribution of OB stars within our survey area. Stars in Fields 1 and 3 are excluded from the histograms. The low-mass stellar distribution is inconsistent with our control group (stars with no lithium detections) even if the region within 1° is excluded, indicative of clustering of the young stars.

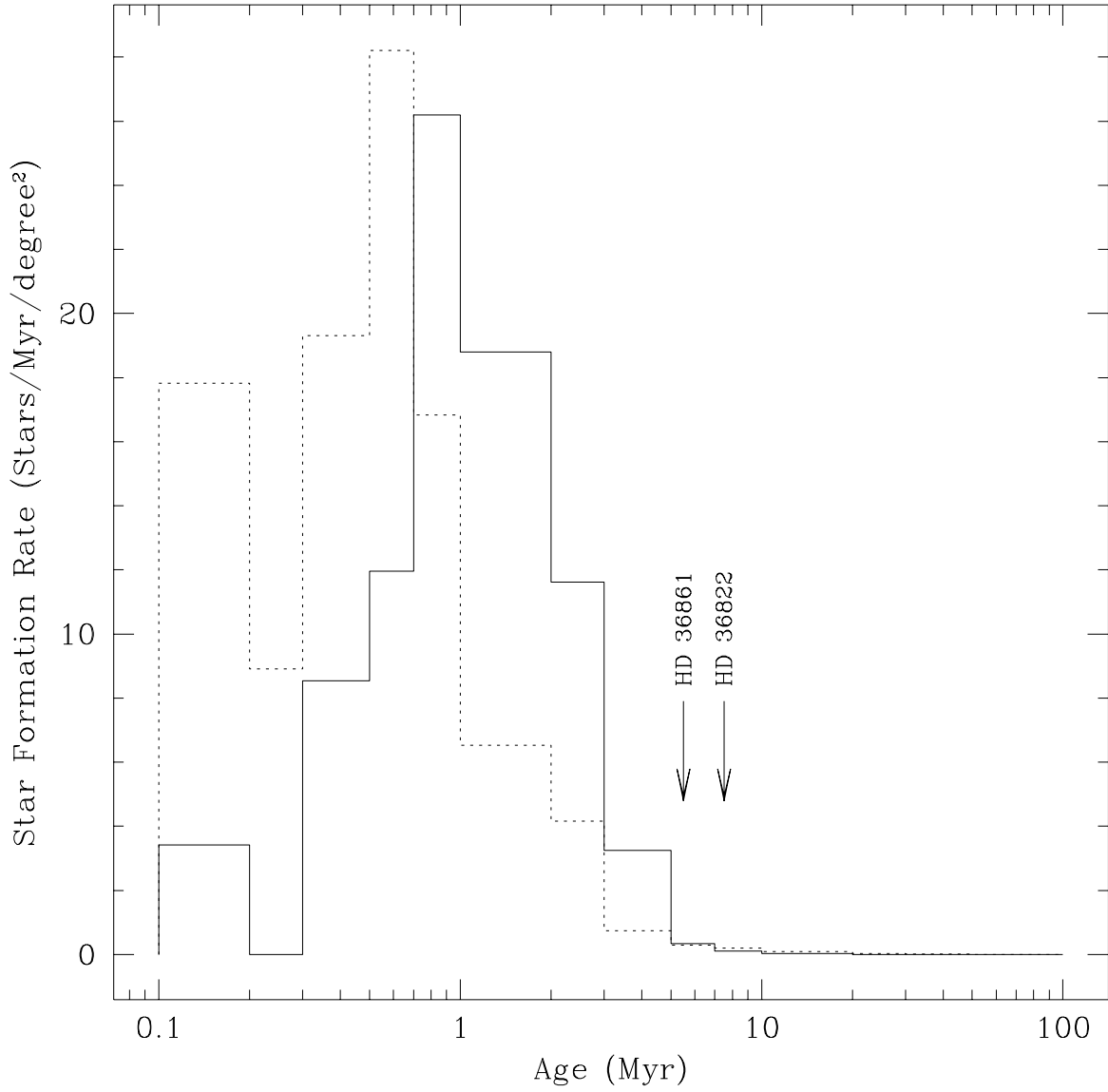


Fig. 10.— Distribution of stellar ages for low-mass PMS stars. The ages derive from comparison to the DM98 model. The individual histograms are composed of stars within 2° radius of λ Ori (solid line) and outside of 2° (dashed line). The arrows mark the ages of the two evolved massive stars.

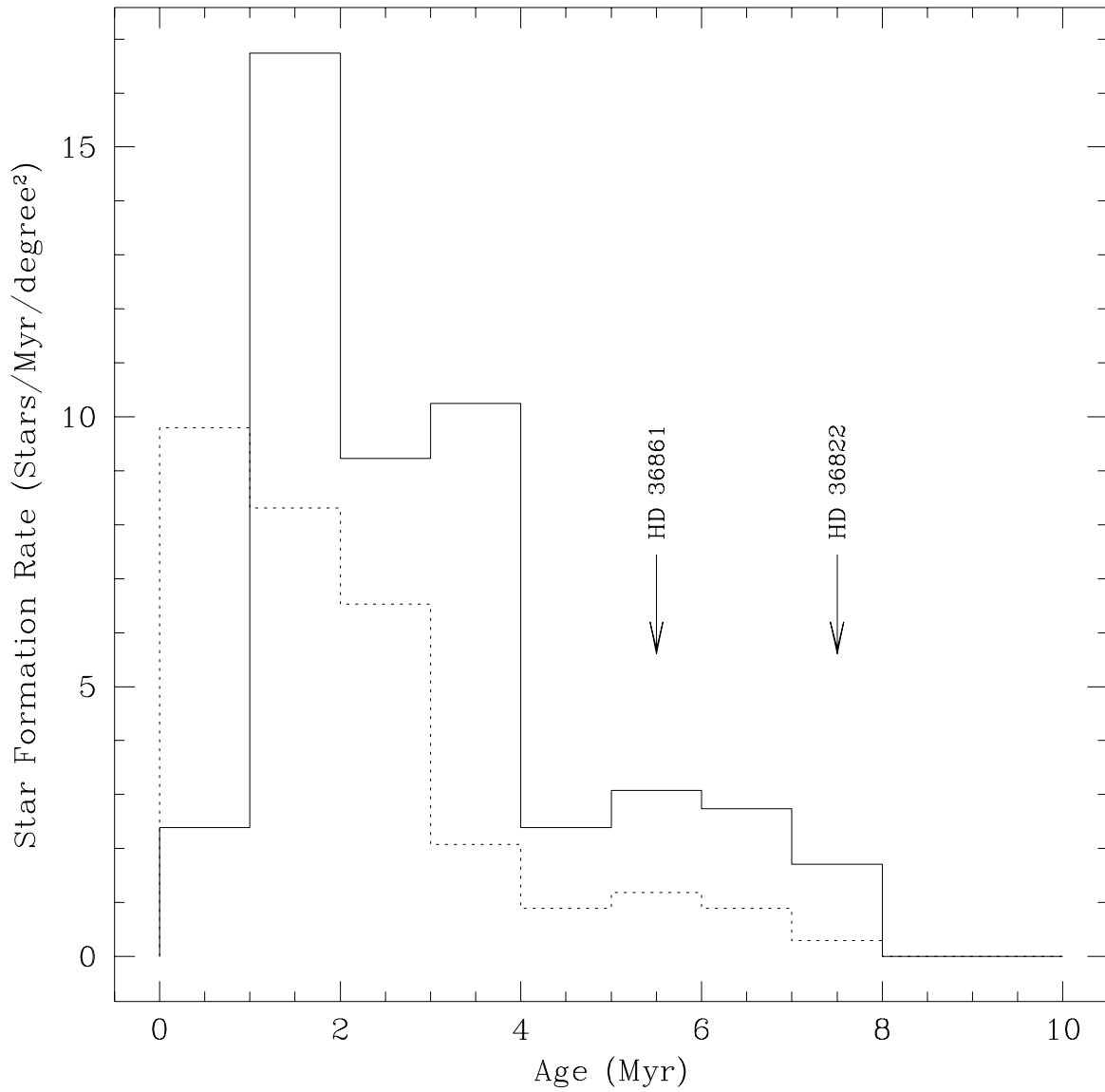


Fig. 11.— Like Figure 10 but for the PS99 model. These histograms are plotted with linear instead of log age for easier comparison with similar plots of Palla & Stahler (2000).

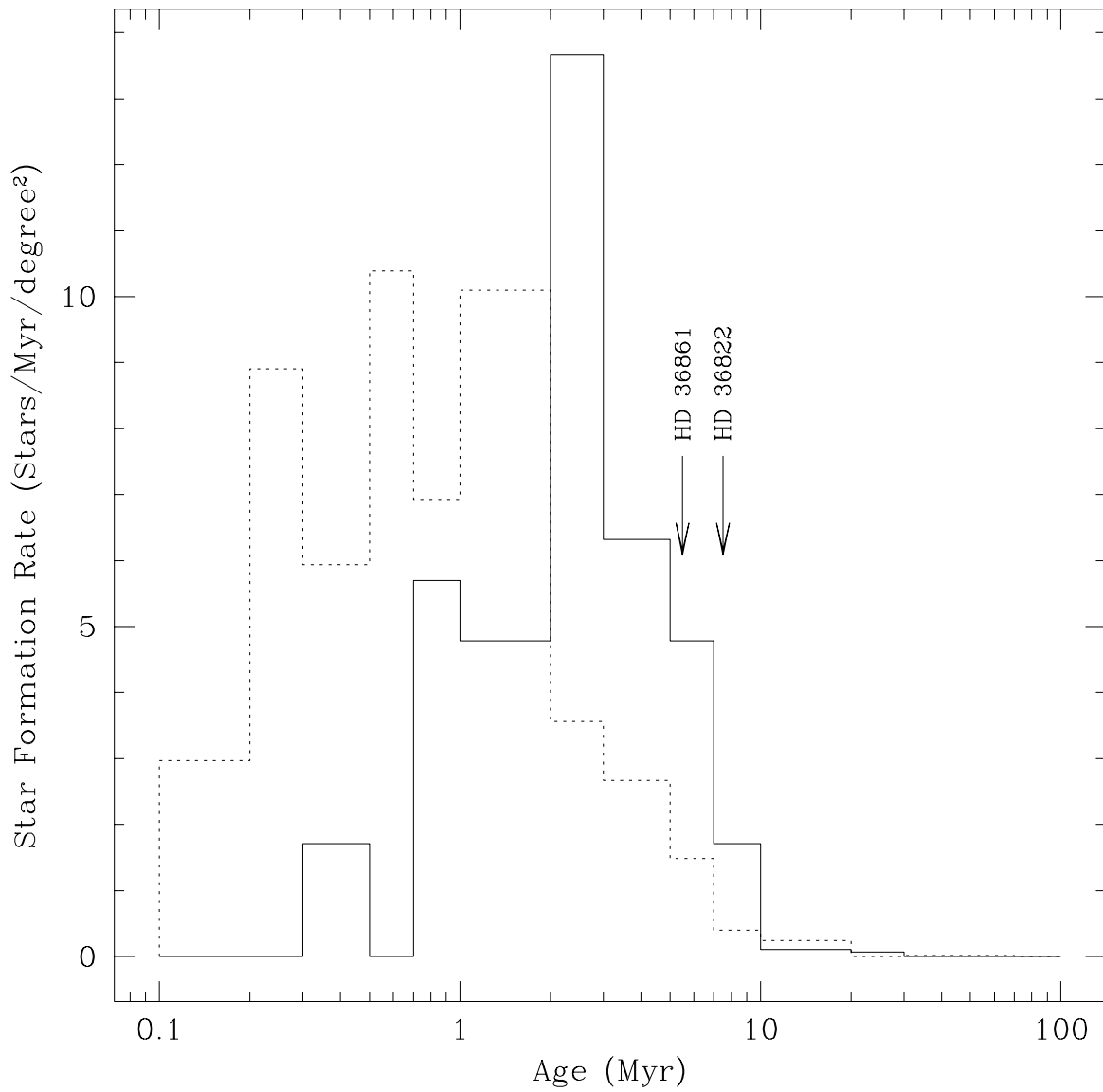


Fig. 12.— Like Figure 10 but for the BCAH98 model.

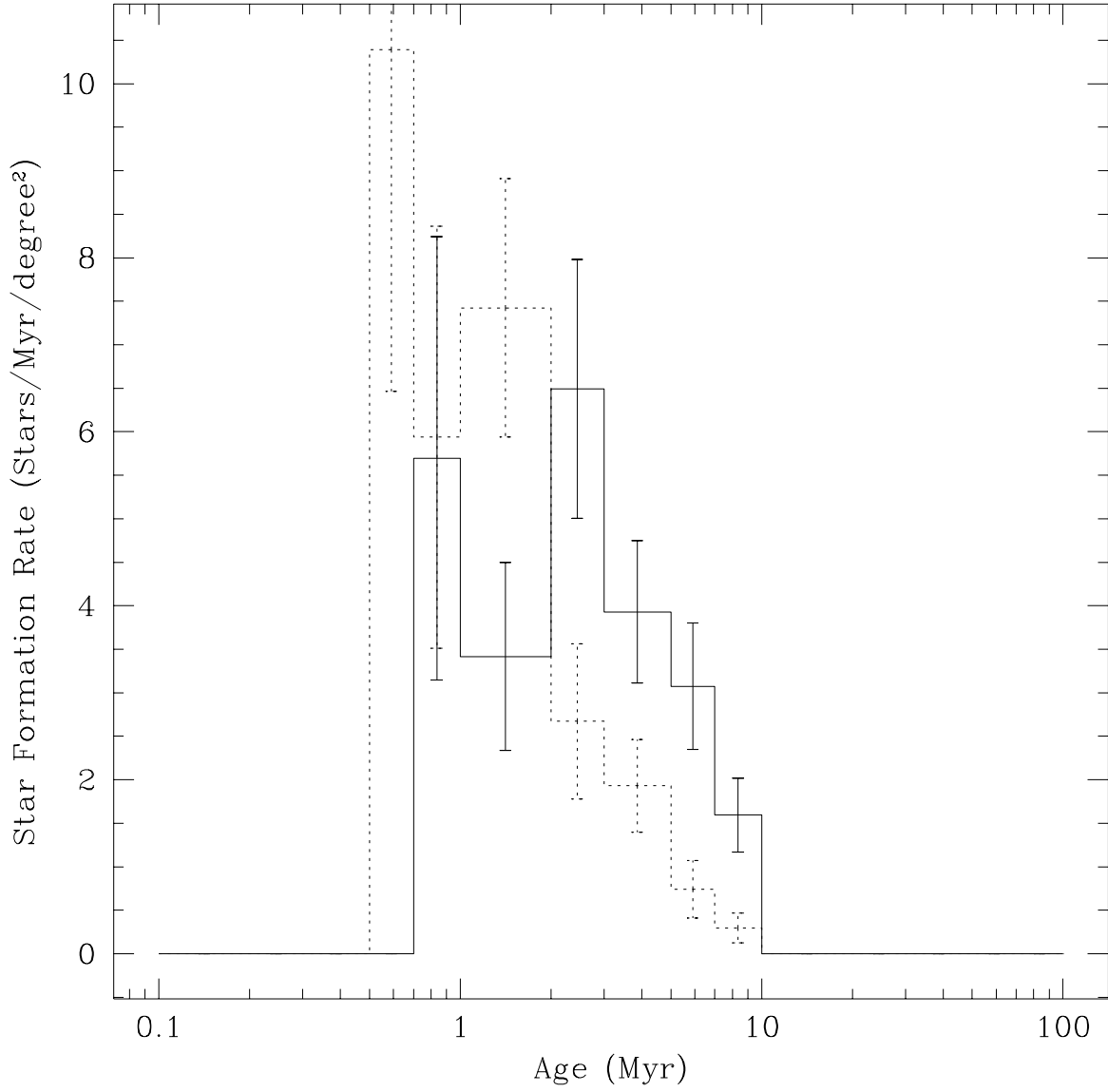


Fig. 13.— Completeness-corrected version of Fig 12. These histograms contain only stars with ages between 0.5 and 10 Myr and masses between 0.55 to $1.2 M_{\odot}$.

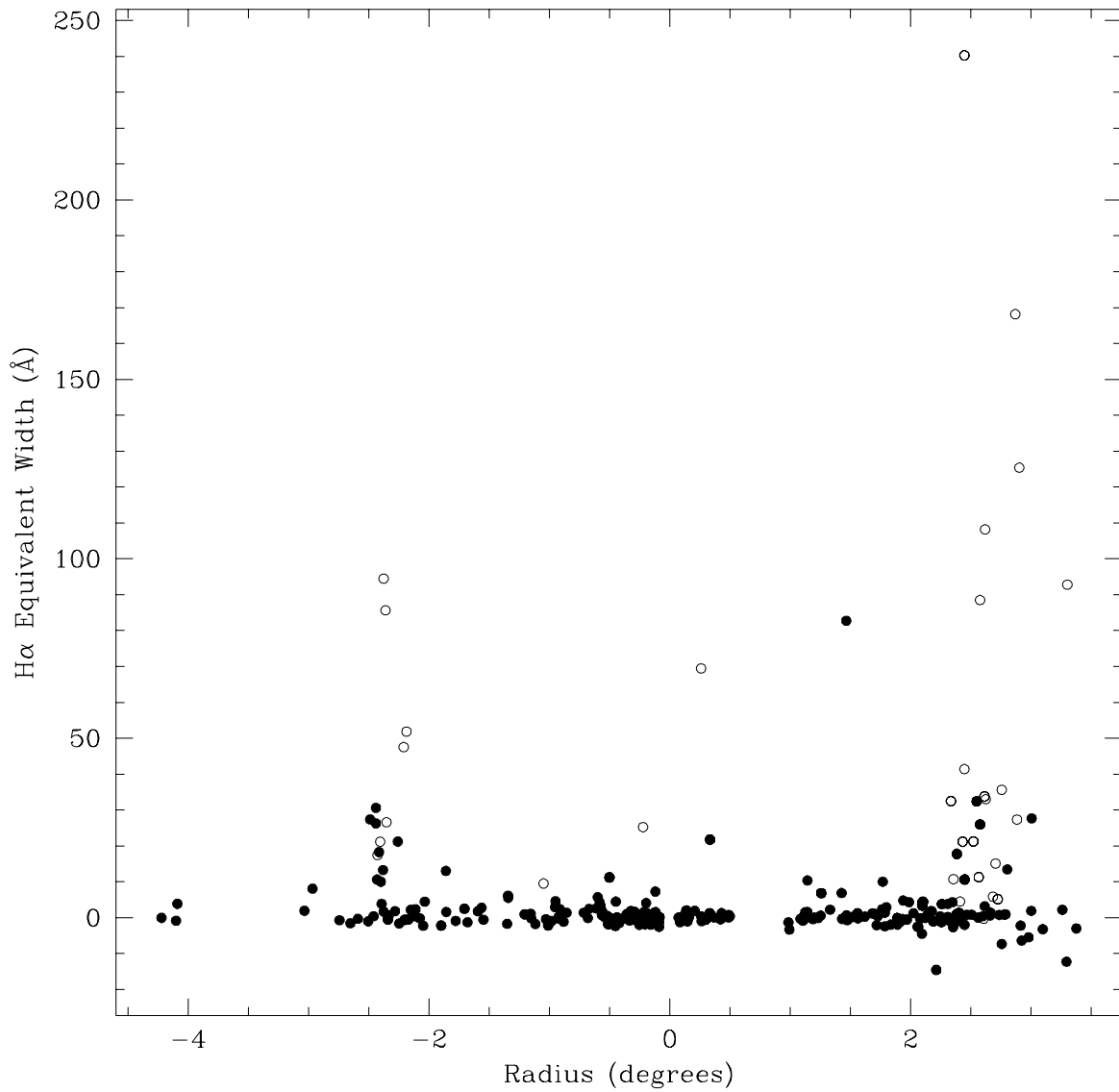


Fig. 14.— Spatial distribution of H α emission. The horizontal axis is the radius from λ Ori with stars to the east marked as negative radius and stars to the west marked as positive radius. Stars which have DIL counterparts are marked as open circles.

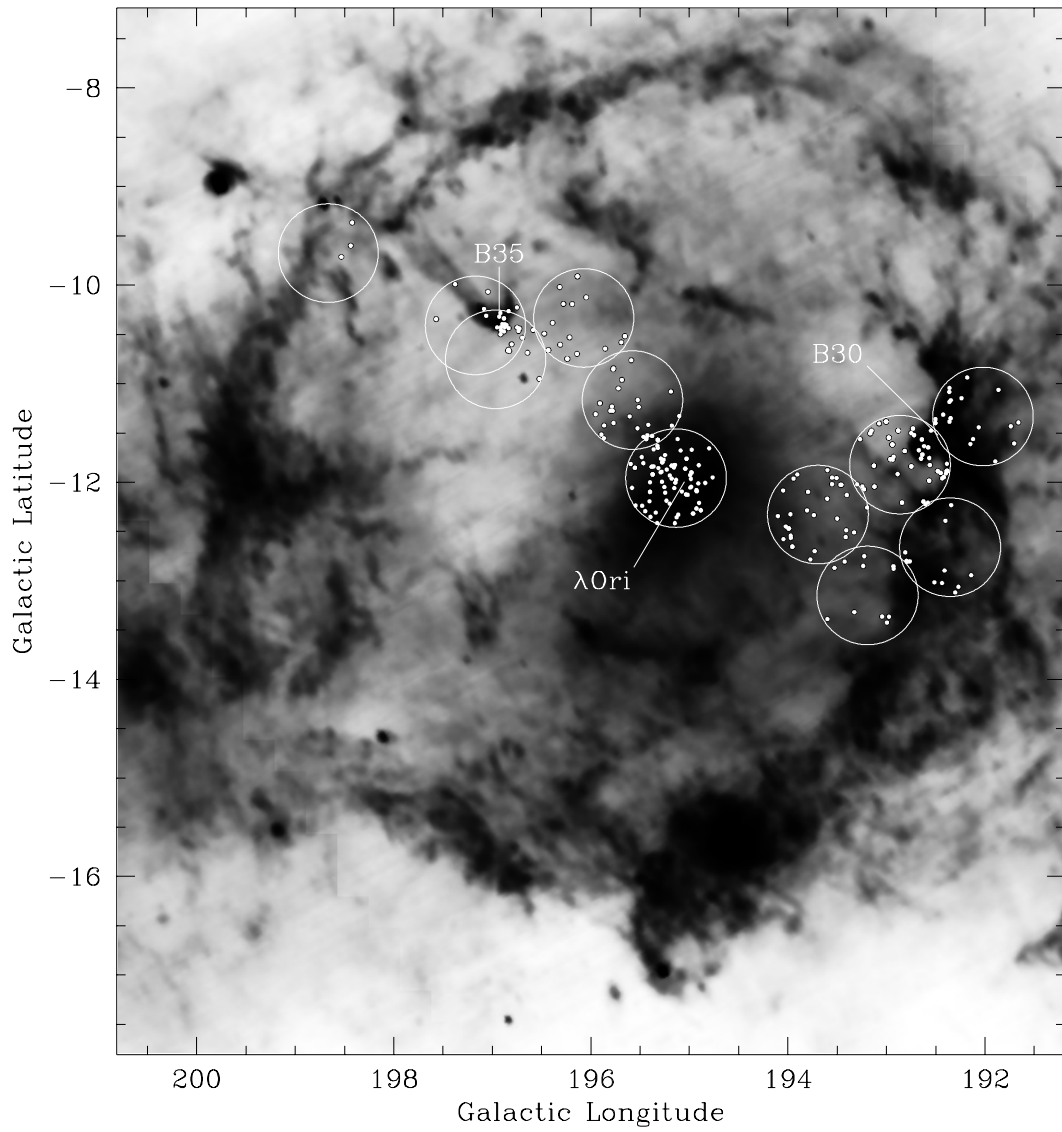


Fig. 15.— Map of our survey PMS stars overlaid on a grayscale IRAS 60- μ m image courtesy of SkyView (McGlynn et al. 1998) on the same scale as Figure 2.